Author Manuscript

Correlation between failure and local material property in chopped carbon fiber chip-reinforced sheet molding compound composites under tensile load

Haibin Tang [a†], Zhangxing Chen [b†], Guowei Zhou [c†], Yang Li [d], Katherine Avery [d], Haiding Guo [a*], Hongtae Kang [e], Danielle Zeng [d], Xuming Su [d]
[a] Jiangsu Province Key Laboratory of Aerospace Power System, Collaborative Innovation Center for Advanced Aero-Engine, Nanjing University of Aeronautics and Astronautics, Nanjing 210016, China
[b] State Key Laboratory of Mechanical Transmission, Chongqing University, Chongqing 400044, China
[c] Department of Mechanical Engineering, University of Michigan, Ann Arbor, 48109, USA
[d] Research and Innovation Center, Ford Motor Company, Dearborn, MI, 48124, USA
[e] Department of Mechanical Engineering, University of Michigan-Dearborn, Dearborn, MI, 48128, USA
† These authors contributed equally to this work.
* Corresponding author. Email: ghd@nuaa.edu.cn

Abstract

To develop further understanding towards the role of a heterogeneous microstructure on tensile crack initiation and failure behavior in chopped carbon fiber chip-reinforced composites, uni-axial tensile tests are performed on coupons cut from compression molded plaque with varying directions. Experimental results indicate that failure initiation is relevant to the strain localization, and a new criterion with the nominal modulus to predict the failure location is proposed based on the strain analysis. Furthermore, optical microscopic images show that the nominal modulus is determined by the chip orientation distribution. At the area with low nominal modulus, it is found that chips are mostly aligning along directions transverse to loading direction and/or less concentrated, while at the area with high nominal modulus, more chips are aligning to tensile direction. On the basis of failure mechanism analysis, it is concluded that transversely-oriented chips or resin-rich regions are easier for damage initiation, while longitudinally-oriented chips postpone the fracture. Good agreement is found among failure mechanism, strain localization and chip orientation distribution.

Key words: chopped carbon fiber chip-reinforced composite; sheet molding compound; failure; strain localization; microstructure

1. Introduction

As promising alternatives to aluminum and steel, high-performance discontinuous fiber or chip reinforced composite materials attract great interest in the automotive industry [1-4]. Chopped chip-reinforced composites, formed by compression molding as a sheet molding compound (SMC), offer a new material molding form for engineering applications. In comparison with traditional continuous fiber composites [5, 6], a chopped material system can achieve a better balance between mechanical performance and manufacturing costs, and it is more suited for complex geometrical structures. Although chopped carbon fiber chip-reinforced materials are commercially-available from various manufacturers, only a limited number of studies focusing on their complicated mechanical behavior have been conducted.

There are several different procedures for chopped carbon fiber chip-reinforced SMC fabrication. One approach is that the chopped chips are scattered into a tray and shuffled to a degree of randomization. Subsequently, the stack of chips is press-molded under elevated temperature and pressure to cure the matrix resin, e.g. carbon/epoxy [1, 7-10] and carbon/polyether-ether-ketone (carbon/PEEK) composites [11-13]. Another similar approach is based on the paper manufacturing technique, e.g. ultra-thin chopped carbon fiber chip-reinforced thermoplastic (UT-CTT) [14-16]. The chopped chips are dispersed in water, and then the water is drained through an aperture on the bottom side, leaving the randomly-oriented chips on a wire net. The chips are then sandwiched between two resin sheets, which are subsequently attached together by heating. A different approach, called the directed carbon fiber preform process (DCFP), is also applied in SMC fabrication [17-20]. Chips are initially deposited onto a region from a revolving chopper head along a series of linear paths. Binder is applied along with the fibers and this process is repeated until the desired fiber areal mass is reached.

Although the discontinuous chips are assumed to be randomly distributed, these materials are actually heterogeneous at the macro-scale level. For example, Feraboli et al. assessed the average elastic modulus of carbon/epoxy composites by strain gage and extensometer, and significant variations in material property at different locations of one specimen were further identified through use of Digital Image Correlation (DIC) [1, 7, 8, 10]. In addition, the effect of chip size and specimen dimension on tensile and compressive properties of this material were quantified experimentally.

This is the author manuscript accepted for publication and has undergone full peer review but has not been through the copyediting, typesetting, pagination and proofreading process, which may lead to differences between this version and the Version of record. Please cite this article as doi:10.1002/pc.24767.

This article is protected by copyright. All rights reserved.

Author Manuscript

Selezneva et al. pointed out that tensile, compressive and shear strength and modulus vary greatly and exhibit dependence on the length of carbon fiber chip for carbon/PEEK composites [11]. Wan et al. conducted a fractographic analysis of UT-CTT, and the result indicates that the obtained elastic modulus is almost independent of both the tape length and molding pressure, while the tensile and compressive strength exhibits high molding pressure sensitivity [14]. Johanson et al. found significant variation in the strain field between two surfaces of DCFP composites during tension after detailed comparison of strain field taken immediately prior to failure [17]. However, further mechanical analysis is needed to describe the specific effects of microstructural variations.

Different advanced testing techniques have been applied to investigate the failure location in composites, including DIC, infrared thermography and X-ray tomography [21]. For chopped chip-reinforced SMC in particular, Feraboli et al. evaluated specimens with pulse-echo C-scan ultrasound as well as pulsed thermography. Several types of defects were detected, such as macro-voids, fiber kinking, swirling or resin-rich areas, but failure may or may not occur in proximity to these hot spots [9]. Johanson et al. pointed out that, at lower applied load, there are so many distinct points with higher-than-average local strain values in the DIC strain images which makes it difficult to identify the failure location [17]. Currently, the failure location in chopped chip-reinforced SMC material still cannot be determined efficiently.

Several researchers have conducted microstructural examination to explore the failure mechanism in chopped chip-reinforced SMC. Based on optical micrographs taken after tensile failure, several phenomena are typically observed: transverse chip cracking, longitudinal chip splitting, chip debonding, and minor digress of fiber breakage [7]. Selezneva et al. claimed that matrix failure is the main cause of failure in tensile tests of carbon/PEEK which occurs in a form of step-wise delamination between chips [11, 22, 23]. In contrast, the observation of UT-CTT conducted by Yamashita et al. shows that fiber breakage, splitting of chips and pulling out of chips are three main failure patterns in tensile fracture [15]. Detailed studies carried out by Johanson et al. indicate that the highest strain concentrations occur at the tip of a longitudinal chip when it coincides with an overlaid transverse one [17]. However, very few works have been done to identify the mechanisms of tensile crack initiation and initial propagation.

The aim of present work is to evaluate the tensile properties of two different types of chopped carbon fiber chip-reinforced SMCs which are formed by a compression molding process. The correlation between strain localization and failure location is explored in detail for quasi-static tensile tests via in-situ DIC. Microstructure characterization is performed at certain locations in tensile-tested samples. Quantitative image analysis is also conducted in order to provide insight into the failure mechanism at the micro-scale. A relationship is established among failure, strain localization and microstructure.

2. Material and experiment setup

2.1. Chopped carbon fiber chip-reinforced SMC molding

Two types of chopped carbon fiber chip-reinforced SMC materials which have different carbon fibers chips and matrix resins are studied. Two different mold geometries are also used, one for each material, which result in significant differences in material flow during molding. An overview of the manufacturing process is shown in Figure 1, as detailed in Ref. [24]. The first SMC material (SMC-A) has a thermoset matrix resin with a glass transition temperature (Tg) in excess of 140°C. The dimensions of the plaques produced of SMC-A are 457.2mm × 457.2mm with thicknesses of 4.8mm. The second SMC material (SMC-B) has a matrix resin with a Tg of less than 140°C. The dimensions of plaques molded in SMC-B are 457.2mm × 304.8mm with thicknesses of 2.4mm. Both SMC-A and SMC-B have similar chip morphologies in the uncured state with a chip length of approximately 25mm. Following molding, the fiber volume fraction is measured by burn off test and density test. The material SMC-A is found to have a fiber volume fraction of 41.8%, while the material SMC-B is found to have a fiber volume fraction of 42.5%.

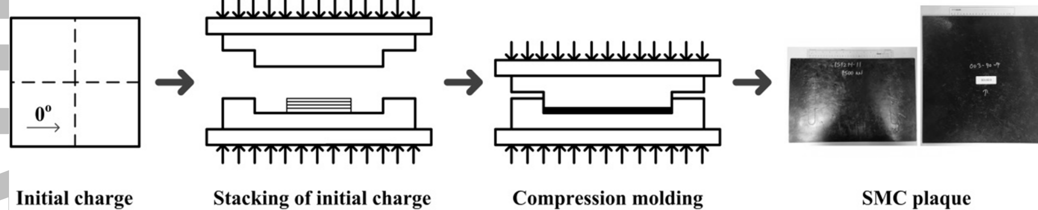

Figure 1. Manufacturing processing of SMC plaque

2.2. Tensile test setup

2.2.1. Tensile test of SMC-A with single-sided DIC

To measure the mechanical properties of chopped carbon fiber chip-reinforced SMC composites,

This article is protected by copyright. All rights reserved.

Author Manuscript

tensile tests with SMC-A samples are performed on a MTS servo hydraulic frame under displacement control at a constant rate of 2mm/min. Tensile sample are prepared according to ASTM D3039 [25], which have dimensions of 203.2mm × 25.4mm. Samples are prepared in three directions (0°, 45° and 90°) as shown in Figure 2 to analyze the extent of anisotropy in the material. Here, the 0° is defined as the direction along a consistent edge of the mold for SMC-A plaques. The strain is measured by a DIC system (ARAMIS), which is calibrated for a measurement area of 175mm × 140mm. To create the pattern for DIC, the samples are first coated with a white spray paint, and then a random pattern of black speckle marks is applied to the surface.

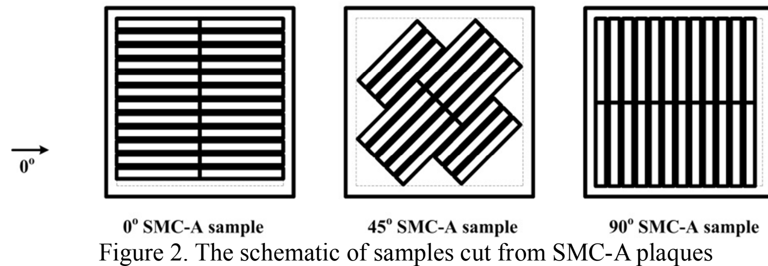

Figure 2. The schematic of samples cut from SMC-A plaques

2.2.2. Tensile test on SMC-A and SMC-B with double-sided DIC

During quasi-static tensile test, strain fields on the opposing sides of SMC samples may not be necessarily the same based on the DIC results of DCFP previously reported [17]. Therefore, a second set of tensile tests are performed on SMC-A and SMC-B which employ two DIC systems to capture the full strain field on opposing faces of the sample simultaneously, as shown in Figure 3. The input force and displacement signals for these two DIC systems are the same. The two systems are aligned by the edge of the painted area, which is strictly controlled to be the same location on both faces. SMC-A samples along 0° direction and SMC-B samples along the 0° and 90° directions, as illustrated in Figure 3, are tested as described above. The 0° direction is defined along the length direction for SMC-B plaques. Due to the difference in plaque dimensions between the molds used for the two materials, some of SMC-B samples are slightly shorter in length (about 177.8mm), which results in a slightly shorter gage section.

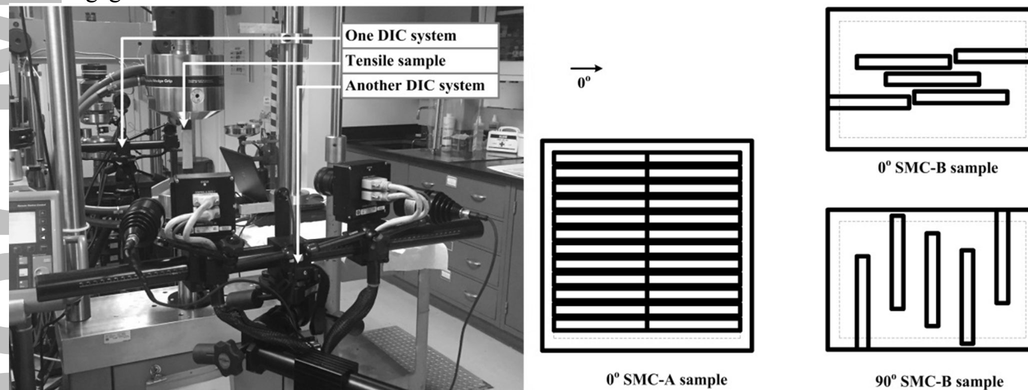

Figure 3. Tensile test set-up with two DIC systems

2.3. Microstructure analysis

Several tested samples from each material are prepared for microstructure analysis, including areas where strain is observed to localize during testing, and where macroscopic cracks are visible. Standard metallographic preparation is used with an automatic system (MuitiPrepTM System 15-2000-GI produced, Allied High Tech Products, Inc.) to remove a precise amount of material from the polished surfaces. Optical microscopy is performed with a Keyence vhx2000 system, and then images are captured and stitched together automatically. Some microscopic images are further processed and analyzed with a MATLAB script for orientation calculation.

This article is protected by copyright. All rights reserved.

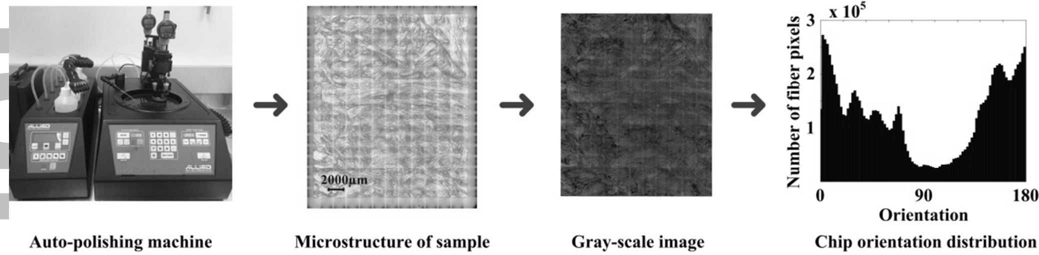

Figure 4. Automatic polishing and image processing

3. Results and discussions

In order to better describe the mechanical characteristics of chopped carbon fiber chip-reinforced composites, several notations are defined in Table 1.

Table 1. Notations of symbol

Symbol	Parameter	Equation	Note
E_{global}	Global modulus	$E_{global} = \frac{\sigma}{\varepsilon_{global}}$	ε_{global} is the surface strain calculated with the whole bar.
$E_{nominal}$	Nominal modulus	$E_{nominal} = \frac{\sigma}{\varepsilon_{local}}$	ε_{local} is the local surface strain calculated with a 1mm×25.4mm (longitudinal length × transverse width) local area.
E_{LNOS}	Low nominal modulus of one side	$E_{LNOS} = (1.0 \sim 1.1) * E_{Lowest-Nominal-One}$	$E_{Lowest-Nominal-One}$ is the lowest $E_{nominal}$ of one side in a sample.
E_{LNTS}	Low nominal modulus of two sides	$E_{LNTS} = (1.0 \sim 1.1) * E_{Lowest-Nominal-Two}$	$E_{Lowest-Nominal-Two}$ is the lowest $E_{nominal}$ of two sides in a sample.
$E_{average}$	Average modulus	$E_{average} = \frac{\sigma}{\frac{\varepsilon_{local} + \varepsilon_{local-oppositing}}{2}} = \frac{2}{\frac{1}{E_{nominal}} + \frac{1}{E_{nominal-oppositing}}}$	$\varepsilon_{local-oppositing}$ and $E_{nominal-oppositing}$ are two values calculated with the oppositing local surface.
E_{LA}	Low average modulus	$E_{LA} = (1.0 \sim 1.1) * E_{Lowest-Average}$	$E_{Lowest-Average}$ is the lowest E_{LA} in a sample.
E_{LN}	Low nominal modulus	$E_{LN} = \sim 0.7 * E_{Average-Nominal}$	$E_{Average-Nominal}$ is the average value of $E_{nominal}$ of all samples for one specific material.
E_{HN}	High nominal modulus	$E_{HN} = \sim 1.3 * E_{Average-Nominal}$	

3.1. Failure location and strain localization from single-sided DIC

Twenty-three valid experiments are obtained from SMC-A samples in section 2.2.1. A representative stress-strain curve for the whole bar is plotted in Figure 5. The stress-strain curve is linear with no distinct yielding or plastic hardening behavior observed before final failure. Tests conducted in the 0°, 45° and 90° directions yield similar results for the ultimate tensile strength (UTS) and global modulus (E_{global}), as shown in Table 2. Therefore, SMC-A appears to feature a random orientation of carbon fiber chips throughout the plaque.

Author Manuscript

This article is protected by copyright. All rights reserved.

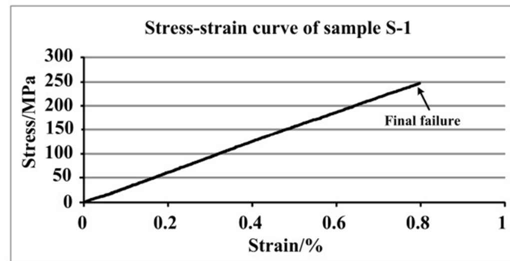

Figure 5. Representative stress-strain curve for the whole bar of SMC-A samples

Table 2. Material property of SMC-A samples

Category	UTS (MPa) / Cov (%)	E_{global} (Gpa) / Cov (%)	# of samples
0°	238 / 8.68	30.7 / 5.92	8
45°	243 / 8.30	30.5 / 5.48	8
90°	252 / 7.57	30.1 / 2.94	7

Figure 6 shows UTS measured for each SMC-A sample, arranged by orientation of the tested sample. Significant variation can be seen in the UTS of SMC-A samples from 200 MPa to 286 MPa. According to fracture observation, crack propagation resulting in the ultimate failure in this chopped chip-reinforced material occurs in only a small part of the whole sample, which is different from that of uni-directional, non-crimp fabric or woven composite materials [6, 26]. Since chopped chip-reinforced composite is heterogeneous at the macro-level, local strain measurement is further explored to identify the failure mechanism.

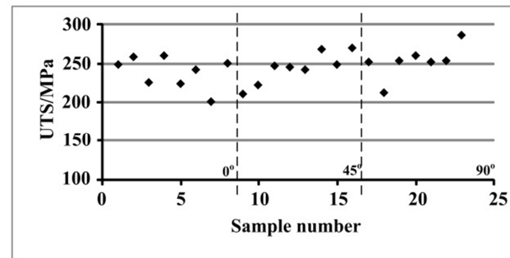

Figure 6. UTS for SMC-A samples

As in prior studies on other chopped carbon fiber chip-reinforced SMCs [1, 11], a significant variation in local strain is observed in the current SMC-A samples. To further examine the relation between local material property and tensile crack initiation, the local strain distribution is analyzed for selected areas with a length of 1mm in the tensile loading direction, as shown in Figure 7(a). Figure 7(b) gives the typical stress-local strain curve at area with high local strain. No distinct modulus degradation is found prior to final failure, and the curves at other local areas of this typical sample are similar. In order to describe the strain localization, the nominal modulus $E_{nominal}$ is used here. Results show that there is an obvious relationship between failure and $E_{nominal}$ for SMC-A samples.

Among twenty-three valid SMC-A samples, seventeen samples are broken at the area with low nominal modulus of one side E_{LNOS}, e.g. sample S-1 shown in Figure 7(c), while other six samples are not, e.g. sample S-2 shown in Figure 7(d). Further, the relationship between UTS and the lowest $E_{nominal}$ of one side at failure location for SMC-A samples is plotted in Figure 8. A trend that the UTS would increase with the growth of the lowest $E_{nominal}$ of one side at failure location can be found for SMC-A materials. It is in agreement with that failure would initiate at the area with E_{LNOS}. Despite the large scatter, a relationship that failure most likely occurs in the location with E_{LNOS} can be achieved.

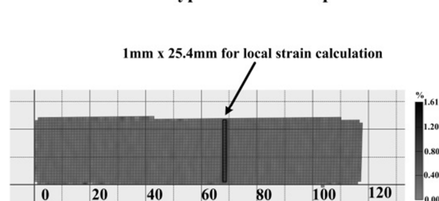

(a)

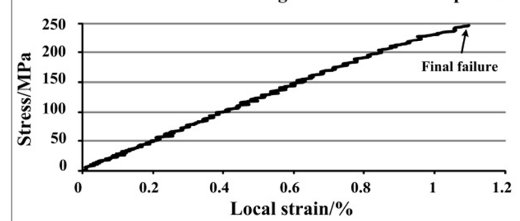

(b)

This article is protected by copyright. All rights reserved.

Author Manuscript

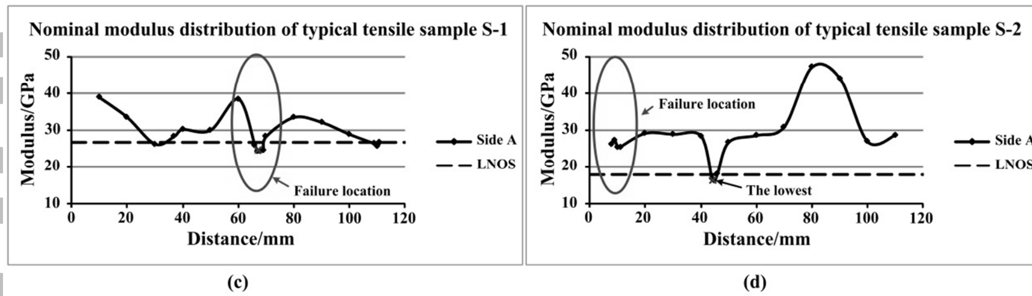

Figure 7. Representative SMC-A samples analysis with strain localization and failure location for (a) an overview of local strain calculation, (b) stress-local strain curve at high strain area, (c) sample S-1, (d) sample S-2.

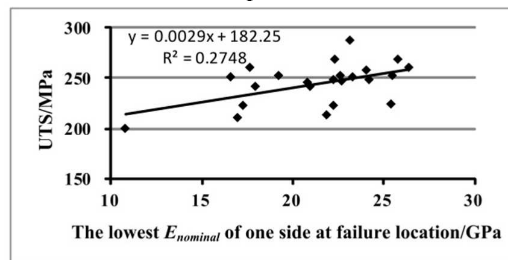

Figure 8. Relationship between UTS and the lowest $E_{nominal}$ of one side at failure location for SMC-A materials.

3.2. Failure location and strain localization from double-sided DIC

Tensile tests with two DIC systems are carried out as described in section 2.2.2. The representative stress-strain curves for the whole bar of SMC-A materials obtained from two opposing sides are nearly the same (Figure 9). Thus, the global modulus calculated with strain captured from each opposing side is similar to the other.

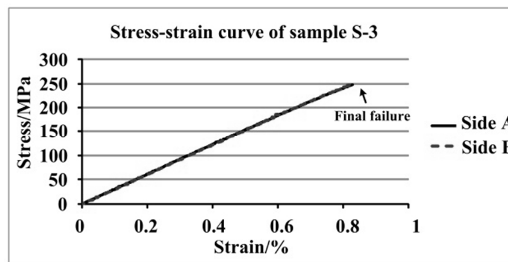

Figure 9. Representative stress-strain curves for the whole bar of SMC-A samples from two opposing sides

For SMC-A materials, eighteen samples are broken at the designed gage section. Due to material heterogeneity, the local strains calculated at different sides or locations are various. The E_{LNOS} can be obtained for two opposing sides, respectively. Note that the lowest values are different for two opposing sides. Results indicate that E_{LNOS} can be observed on at least one side of sample at the failure location for all valid data. Further, the correlation between tensile failure and the local strain measured by either side or the average strain calculated by two sides is discussed in detail.

The low nominal modulus of two sides E_{LNTS} and the low average modulus E_{LA} are proposed here. Experimental results show that eleven of eighteen SMC-A samples fail at locations with both E_{LNTS} and E_{LA}, e.g. sample S-4 in Figures 10(a). Among the rest of the SMC-A samples, three samples fail only at the location with E_{LA}, e.g. sample S-5 in Figure 10(b), while another three samples fail only at the location with the E_{LNTS}, and e.g. sample S-6 shown in Figure 10(c). Only one sample that is sample S-7 shown in Figure 10(d) does not fit for both criteria. Therefore, both E_{LNTS} and E_{LA} can be used to locate the potential failure site for SMC-A materials. The relationship between modulus at failure location and UTS for SMC-A materials is plotted in Figures 11(a) and (b), respectively. A slightly better correlation between UTS and the lowest average modulus at failure location can be found for SMC-A materials.

This article is protected by copyright. All rights reserved.

Author Manuscript

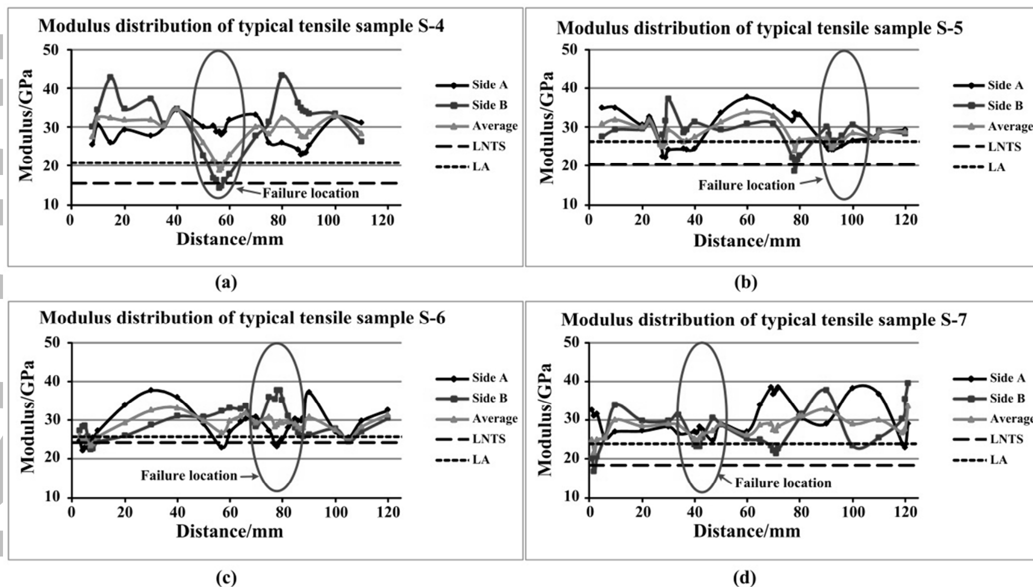

Here, E_{LNTS} is below the LNTS line (1.1 × the lowest $E_{nominal}$ of two sides).
E_{LA} is below the LA line (1.1 × the lowest $E_{average}$).

Figure 10. Representative SMC-A samples analysis with strain localization and failure location for (a) sample S-4, (b) sample S-5, (c) sample S-6, and (d) sample S-7

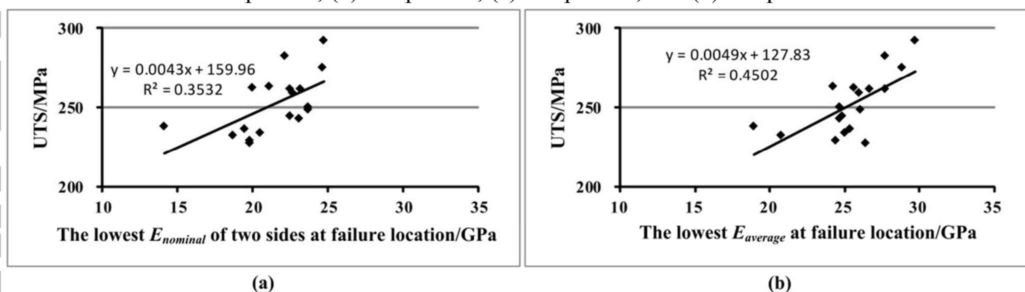

Figure 11. Relationship between UTS and modulus for SMC-A materials for (a) the lowest $E_{nominal}$ of two sides at failure location and (b) the lowest $E_{average}$ at failure location

For SMC-B materials, ten samples fail at the gage section. Similar to SMC-A materials, the representative stress-strain curves for the whole bar of SMC-B materials obtained from two opposing sides are also very close (Figure 12). Generally, the failure strain of SMC-B materials is much smaller than that of SMC-A. Some samples (e.g. sample S-8) exhibit a decrease in global modulus prior to failure, while some samples (e.g. sample S-9) do not. SMC-B samples cut from different locations and directions, and the results show great variations for these samples in global modulus, which range from 17.6GPa to 38.3Gpa, as given in Figure 13. Unlike SMC-A material, dimension of SMC-B plaques along 0° and 90° directions are not the same. Therefore, the material flow during compression molding is not isotropic. Since the material flow along 0° direction is stronger than 90° direction, distribution of directions of fiber chips are biased towards 0° direction at all locations of the plaque, which explains 0° samples generally have a higher global modulus compared to 90° ones.

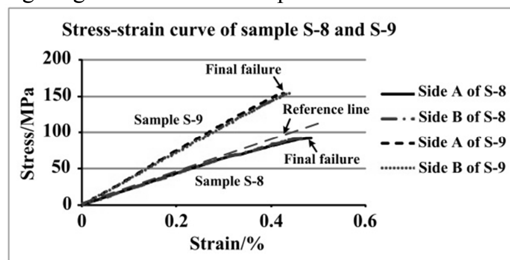

Figure 12. Representative stress-strain curves for the whole bar of SMC-B samples from two opposing sides

This article is protected by copyright. All rights reserved.

Author Manuscript

Author Manuscript

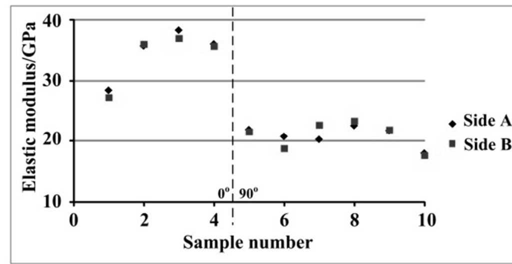

Figure 13. Global modulus for SMC-B materials

Similarly, E_{LNOS} also can at least be observed at one side of failure location for all SMC-B samples. E_{LNTS} is applicable for seven SMC-B samples to locate the failure position, while E_{LA} is applicable for all valid SMC-B data. Two typical SMC-B samples S-10 and S-11 are shown in Figures 14(a) and (b), respectively. Here, sample S-10 fails at the location with both E_{LNTS} and E_{LA}, but sample S-11 fails only at the location with E_{LA}. The relationship between modulus at failure location and UTS for SMC-B materials is summarized in Figure 15. In particular, the linear relation between UTS and lowest $E_{average}$ at failure location is observed. By comparison, the average modulus $E_{average}$ is more suitable in terms of predicting the final failure location for SMC-B materials.

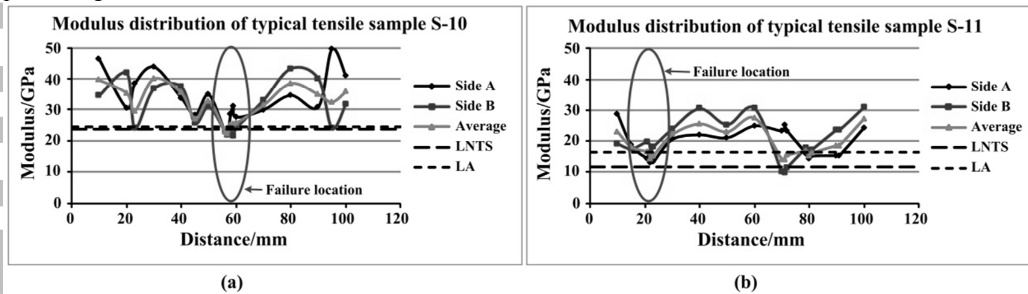

Here, E_{LNTS} is below the LNTS line (1.1 × the lowest $E_{nominal}$ of two sides).
E_{LA} is below the LA line (1.1 × the lowest $E_{average}$).

Figure 14. Representative SMC-B samples analysis with strain localization and failure location for (a) sample S-10 and (b) sample S-11

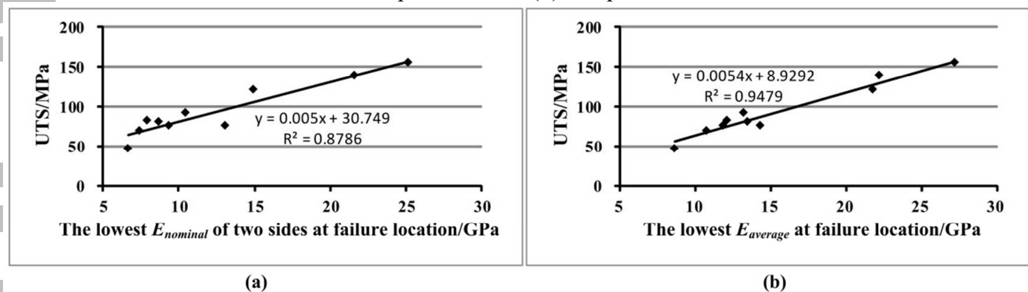

Figure 15. Relationship between UTS and modulus for SMC-B materials for (a) the lowest $E_{nominal}$ of two sides at failure location and (b) the lowest $E_{average}$ at failure location

Based on the analysis with SMC-A and SMC-B materials, there is a general correlation between failure location and E_{LA} for chopped carbon fiber chip-reinforced SMC composites. The crack initiation and propagation are determined by the local material property, which can be characterized by $E_{average}$. In Johanson's work [17], the local concentration points cannot be used to predict the failure location. However, based on our work, detailed analysis on strain localization, i.e. $E_{nominal}$ and $E_{average}$, can reliably predict final failure even at low applied loads.

3.3. Strain localization and microstructure

Due to the relationship between failure location and strain localization for chopped carbon fiber chip-reinforced SMC materials, the microstructure of skin layers is examined for failure analysis. On the basis of DIC data, different nominal modulus can be found at the local section of chopped carbon fiber chip-reinforced SMC materials. After tensile tests, several representative samples corresponding to area with low nominal modulus E_{LN} and high nominal modulus E_{HN} are cut from SMC-A samples and polished to obtain the microstructure information of skin layers, e.g. areas marked by rectangular in Figure 16 (a) and (b).

This article is protected by copyright. All rights reserved.

Author Manuscript

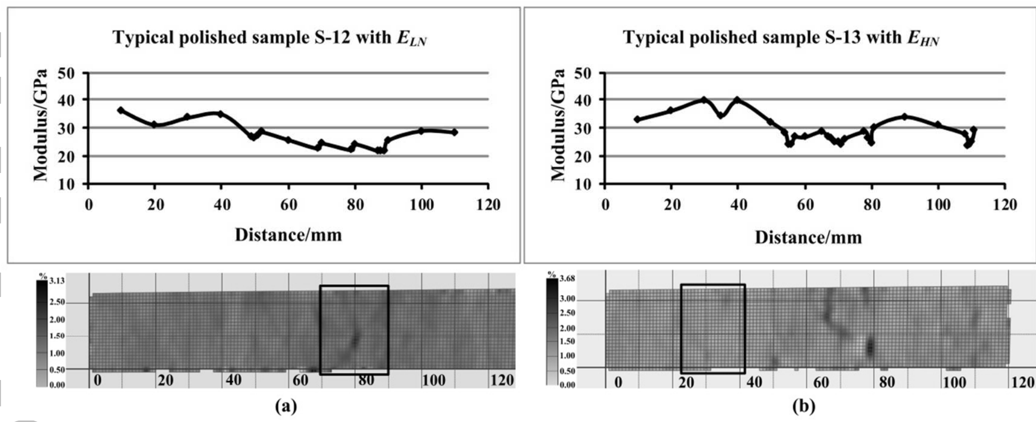

Figure 16. Representative sample for microstructure analysis for (a) sample S-12 with E_{LN} and (b) sample S-13 with E_{HN}

Areas with E_{LN} tend to have a chip orientation transverse to the loading direction, while areas with E_{HN} tend to have chips more aligned with the loading direction, e.g. two typical layers in Figure 17(a) and (b). In order to quantify the chip orientation distribution of these samples, the fiber orientation tensors in microstructure images are analyzed in current work following a computer vision algorithm originally developed for the fingerprints analysis [27, 28]. The aligned original images are converted into a gray-scale style and denoised using the median filter. The individual fibers in the chips are recognized and the tangential direction of the fiber is measured at each pixel that belongs to this fiber. Histogram of the pixel-wise tangential directions are then plotted used to calculate the fiber orientation tensor a_{ij} defined in Ref. [29]. Very few out-of-plane chips are observed in all of the chopped carbon fiber chip-reinforced SMC plaques in this work as the in-plane dimensions of the plaque are considerably larger than the plaque thickness, so planar fiber orientation tensor is sufficient to describe the chip orientation distribution. In Cartesian coordinate system (Figure 18), the orientation of a single chip can be represented by a unit vector $\boldsymbol{p}=(p_1, p_2)$, which is calculated by:

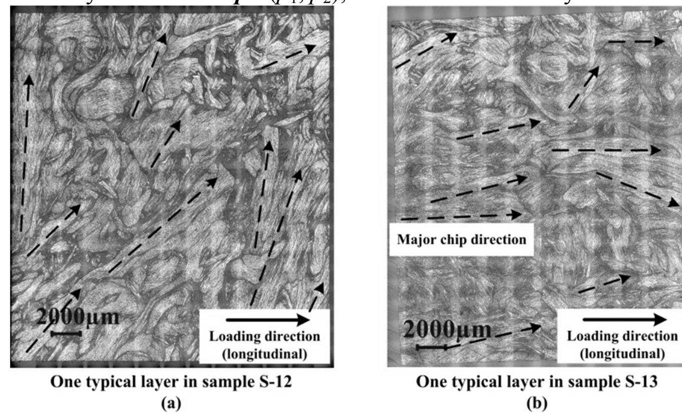

Figure 17. Typical microstructures for sample in Figure 16 for (a) sample S-12 with E_{LN} and (b) sample S-13 with E_{HN}

$$p_1 = \cos\Phi \qquad (1)$$
$$p_2 = \sin\Phi$$

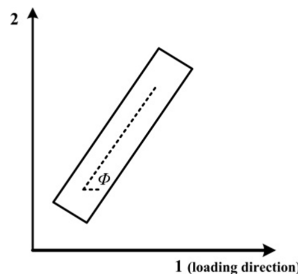

Figure 18. Coordinate system and definition of Φ

The commonly used second-order fiber orientation tensor is listed below, which is calculated as:

This article is protected by copyright. All rights reserved.

$$a_{ij} = \int_0^{2\pi} p_i p_j \psi(\Phi) d\Phi = \sum_{k=1}^{180} p_i p_j \frac{n_k}{n_{total}} \qquad (i, j = 1, 2) \tag{2}$$

Here, $\Psi(\Phi)$ is the distribution function, n_k is the number of fiber pixels along direction of k degree (range from 1 to 180), and n_{total} is the total number of the fiber pixels in the microstructure image.

The corresponding chip orientation distribution and fiber orientation tensors in Figure 17 are presented in Figure 19 (a) and (b). The relationship between average a_{11} and $E_{nominal}$ for polished samples is listed in Figure 20. The calculated $E_{nominal}$ is directly determined by the chip orientation distribution of skin layers, and a positive correlation between strain localization and microstructure can be concluded. It should be noted that the local fiber volume fraction also has certain influence on the calculated nominal modulus. In addition, some areas with very low $E_{nominal}$ are also polished for SMC-B materials for further comparison, and resin-rich regions are sometimes observed (Figure 21). The $E_{nominal}$ would reduce with the decrease of local fiber volume fraction.

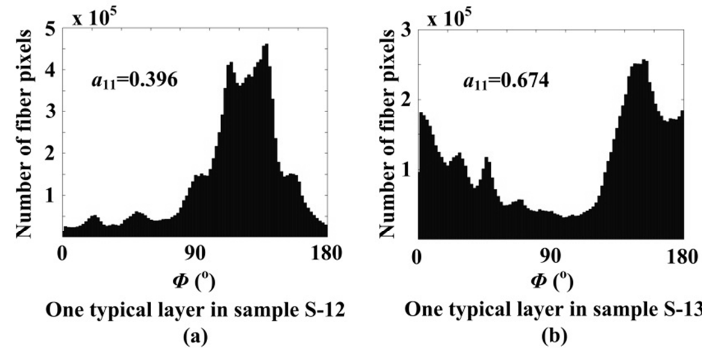

Figure 19. Chip orientation distribution and the calculated a_{11} components of the fiber orientation tensors of images in Figure 17 for (a) sample S-12 with E_{LN} and (b) sample S-13 with E_{HN}

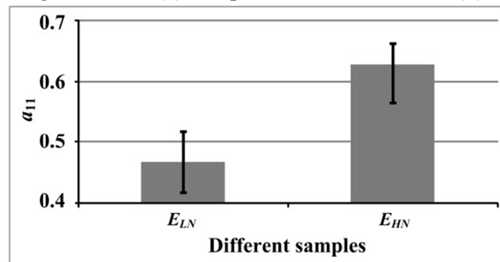

Figure 20. Relationship between average a_{11} and $E_{nominal}$

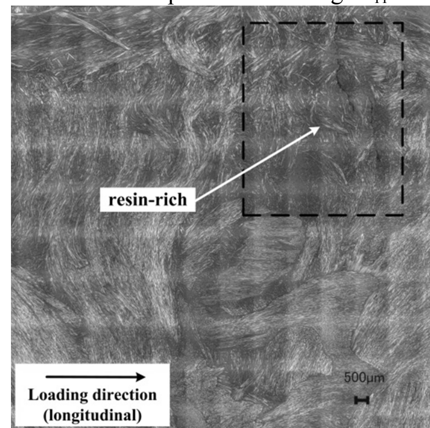

Figure 21. Resin-rich region in SMC-B materials

3.4. Failure and local microstructure

In order to thoroughly understand the failure mechanism under tensile loading condition, the crack initiation and initial propagation are explored in this section. For chopped carbon fiber chip-reinforced SMC composites, the dominate crack only occurs at one small location of the whole sample, while sometimes minor cracks can also be observed simultaneously at other locations (Figure 22). As limited information about the processing of crack initiation and initial propagation can be obtained from the

This article is protected by copyright. All rights reserved.

Author Manuscript

Author Manuscript

fully failed locations, several cracks away from the final failure location are polished to examine the relationship between failure and local microstructure.

Figure 22. Dominate and minor cracks

For one typical polished sample S-14 (red rectangular area in Figure 23), very high local strain concentration is observed from the DIC images which are captured just prior to final failure. After the first layer (layer 1) that is about 200μm below the surface is obtained, sample S-14 is further removed another 70μm (layer 2), 50μm (layer 3) along thickness direction to get more microstructure information. Here, three significant locations with cracks namely A-C are studied as illustrated in Figure 24(a), (b) and (c). In order to quantify the specific chip or crack direction, the angle Φ defined in Figure 18 is used below.

At location A, a transverse crack occurs at the edge of a transverse chip and the end of a 110° tilted chip. It should be noted that cracks are confirmed by the microstructure comparison of different layers. Because the diameter of single fiber is only approximately 7μm, this approach is efficient to eliminate the confusion of fiber dropping off. At location B, 135° tilted cracks are along the edge of chips as well as inside chips. At location C, another transverse crack appears at the end of a longitudinal chip and the edge of a 100° tilted chip. In addition, no crack is found at the location C in the image of layer 1, which indicates that the cracks of SMC materials initiate not only at the surface but also at the skin layers.

The polished location is still at the crack initiation and initial propagation processing. Along the critical cross section, including location A-C, further crack bridging can be expected in the propagation processing.

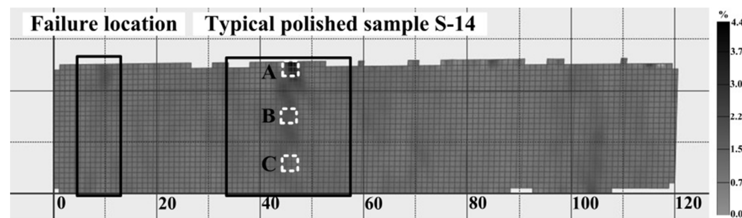

Figure 23. Typical sample for failure analysis

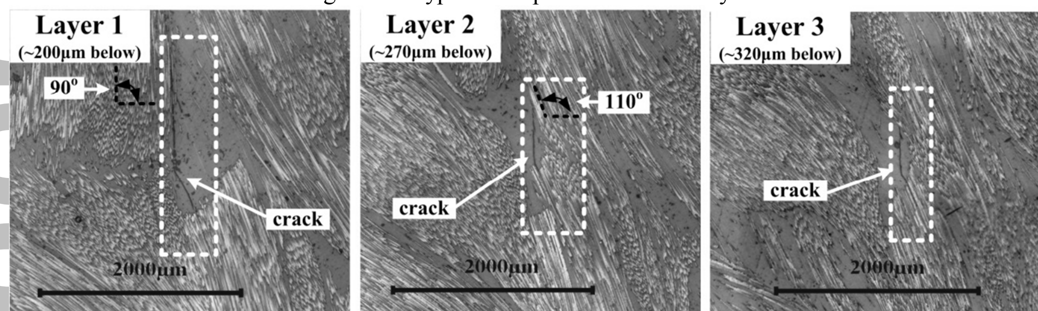

(a)

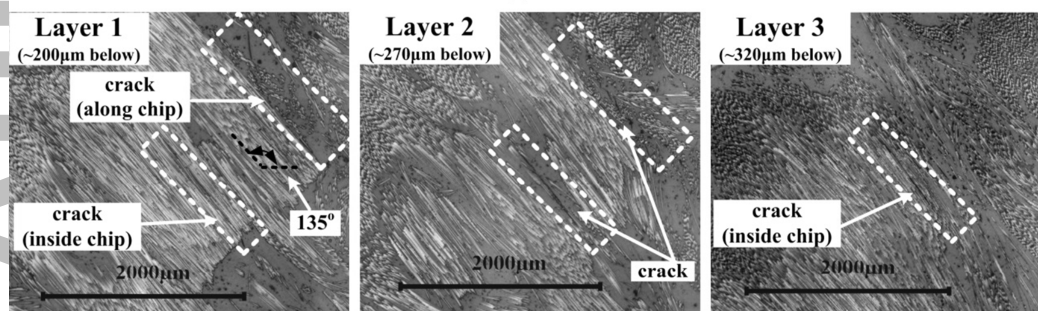

(b)

This article is protected by copyright. All rights reserved.

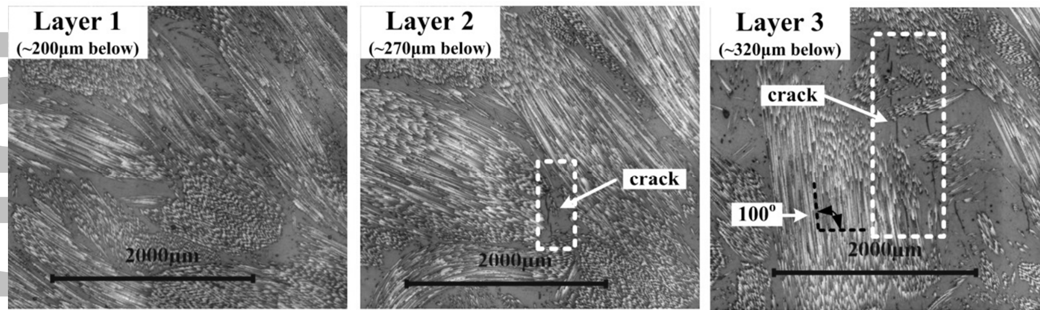

(c)

Figure 24. Crack initiation and initial propagation at different locations in sample S-14 for (a) location A, (b) location B, and (c) location C

For another typical polished sample S-15, there is a macro-crack after tensile test, as shown in Figure 25. Similarly, after the first layer (layer 1) that is about 200μm below the surface is captured, sample S-15 are further removed another 100μm (layer 2), 150μm (layer 3) and 150μm (layer 4), respectively. The microstructures of four representative layers are illustrated in Figure 26(a), (b), (c) and (d), and three areas with crack namely A-C is discussed in detail.

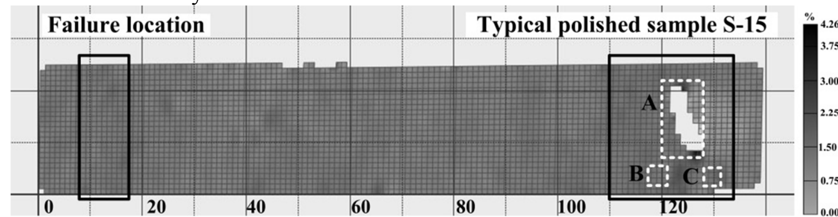

Figure 25. Typical polished sample S-15

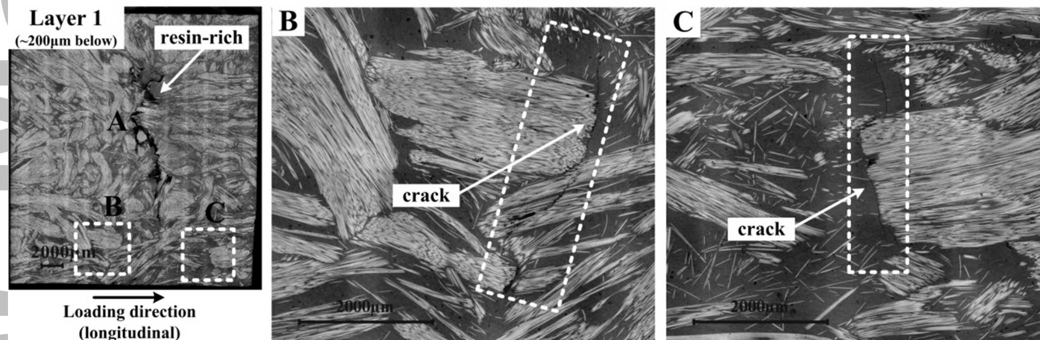

(a)

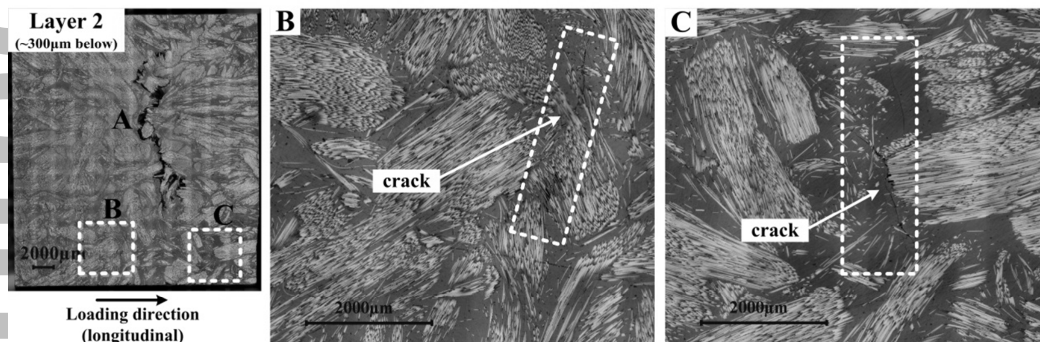

(b)

This article is protected by copyright. All rights reserved.

Author Manuscript

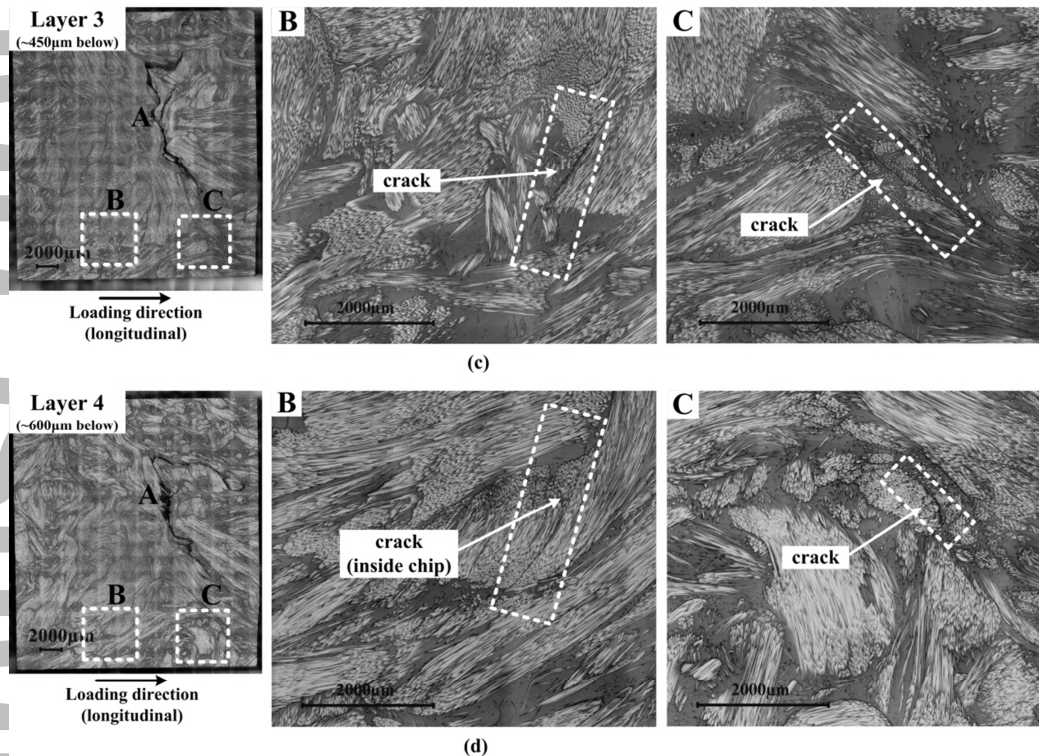

Figure 26. Microstructure of sample S-15 at different layers for (a) layer 1, (b) layer 2, (c) layer 3, and (d) layer 4.

At location A, a large macro-crack can be found obviously at different skin layers. The crack propagates along the edge of several chips close to transverse direction. Local resin-rich region is also observed at location A. At location B and C, two cracks appear at the end of longitudinal chips, along the edge of tilted chips and inside tilted chips. An uncommon phenomenon should be pointed out that the crack in location B crosses the neighboring chip at the layer 1, which is seldom observed in other layers or samples.

In summary, cracks usually initiate at the end of longitudinal chips as well as inside or at the edge of chips along or close to the transverse direction, and cracks propagate in adjacent layers in this initiation processing. If chips are along or close to transverse direction more cracks would initiate. In the propagation procedure, it could be expected that more energy would be absorbed if cracks cross chips or propagate along a long path to pass by chips. If chips are along or close to transverse direction cracks would be much easier to propagate. In addition, resin area is also highly susceptible to crack initiation and initial propagation. It should be pointed out the relationship between failure mechanism and microstructure agrees with the correlation between failure and strain localization as well as that between strain localization and microstructure.

4. Conclusions

The mechanical properties and failure mechanism of compression molded SMC composed of chopped carbon fiber chip-reinforced composites under tensile loading condition have been experimentally investigated in this paper. Uni-axial tensile tests are performed on coupons cut from compression molded plaque with local strain analysis by DIC systems. Microstructure characterization utilizing state-of-art image analysis is then followed to examine the material variation as well as the initiation of cracks. Results of tensile experiments indicate that failure initiation coincides with a strain localization observable from one or both sides of a tested sample. $E_{nominal}$ and $E_{average}$ are found to be good indicators of tensile failure. Optical microscopic images show that $E_{nominal}$ is determined by the chip orientation distribution. At area with E_{LN}, it is found that chips are mostly aligning along directions transverse to loading direction and/or less concentrated, while at area with E_{HN}, more chips are aligning to tensile direction. On the basis of failure mechanism analysis, it is concluded that transversely-oriented chips or resin-rich regions are easier for damage initiation, while longitudinally-oriented chips postpone the fracture. Good agreement is found among failure mechanism, strain localization and chip orientation distribution.

This article is protected by copyright. All rights reserved.

Author Manuscript

Author Manuscript

Acknowledgements
This research is supported by Ford Motor Company. The authors gratefully acknowledge the contribution of Dr. L. Huang and Dr. Carlos Engler-Pinto for the detailed discussion of this work.

Reference

[1] Feraboli P., Peitso E., Cleveland T. Modulus measurement for prepreg-based discontinuous carbon fiber/wpoxy systems. J Compos Mater. 2009;43: 1947-1965.

[2] Chen L., Gu B. Predicting fatigue damage in interphase of short fiver reinforced rubber composites under transverse load. Polym Composite. 2016.

[3] Law T.T., Phua Y.J. Senawi R., Hassan A., Mohd Ishak Z.A. Experimental analysis and theoretical modeling of the mechanical behavior of short glass fiber and short carbon fiber reinforced polycarbonate hybrid composites. Polym Composite. 2016;37: 1238-1248.

[4] Tseng H.C., Chang R.Y., Hsu C.H. Accurate predictions of orientation dependent modulus in short-fiber-reinforced composite with experimental validation. Polym Composite. 2017.

[5] Sun W., Vassilopoulos A.P., Keller T. Experimental investigation of kink initiation and kink band formation in unidirectional glass fiber-reinforced polymer specimens. Compos Struct. 2015;19: 9-17.

[6] Ma Y., Ueda M., Yokozeki T., Sugahara T., Yang Y., Hamada H. A comparative study of the mechanical properties and failure behavior of carbon fiber/epoxy and carbon fiber/polyamide 6 unidirectional composites. Compos Struct. 2017;160: 89-99.

[7] Feraboli P., Peitso E., Deleo L., Cleveland T. Characterization of prepreg-based discontinuous carbon fiber/epoxy systems. J Reinf Plast Compos 2009;28: 1191-1214.

[8] Feraboli P., Peitso E., Cleveland T., Stickler P.B., Halpin J.C. Notched behavior of prepreg-based discontinuous carbon fiber/epoxy systems. Compos Part A-Appl S. 2009;40: 289-299.

[9] Febraboli P., Cleveland T., Ciccu M., Stickler P., Deoto L. Defect and damage analysis of advanced discontinuous carbon/epoxycomposite materials. Compos Part A-Appl S. 2010;41: 888-901.

[10] Febraboli P., Cleveland T., Stickler P., Halpin J. Stochastic laminate analogy for simulating the variability in modulusof discontinuous composite materials. Compos Part A-Appl S. 2010;41: 557-570.

[11] Selezneva M., Lessard L. Characterization of mechanical properties of randomly oriented strand thermoplastic composites. J Compos Mater. 2016;50: 2833-2851.

[12] Landry B., Hubert P. Experimental study of defect formation during processingof randomly-oriented strand carbon/PEEK composites. Compos Part A-Appl S. 2015;77: 301-309.

[13] Martel G.P.P., Levy A., Hubert P. Compression moulding of Carbon/PEEK Randomly-Oriented Strandscomposites: A 2D Finite Element model to predict the squeeze flowbehaviour. Compos Part A-Appl S. 2016;81: 69-77.

[14] Wan Y., Takahashi J. Tensile and compressive properties of chopped carbon fiber tapes reinforced thermoplastics with different fiber lengths and molding pressures. Compos Part A-Appl S. 2016;87: 271-281.

[15] Yamashita S., Hashimoto K., Suganuma H., Takahashi J. Experimental characterization of the tensile failure mode of ultra-thin chopped carbon fiber tape-reinforced thermoplastics. J Reinf Plast Compos. 2016;35: 1342-1352.

[16] Wan Y., Straumit I., Takahashi J., Lomov S.V. Micro-CT analysis of internal geometry of chopped carbon fiber tapes reinforced thermoplastics. Compos Part A-Appl S. 2016;91: 211-221.

[17] Johanson K., Harperl L.T., Johnson M.S., Warrior N.A. Heterogeneity of discontinuous carbon fibre composites: damageinitiation captured by digital image correlation. Compos Part A-Appl S. 2015;68: 304-312.

This article is protected by copyright. All rights reserved.

[18] Harper L.T., Turner, T.A., Warrior N.A., Rudd C.D. Characterisation of random carbon fibre composites from adirected fibre preforming process: the effect of fibre length. Compos Part A-Appl S. 2006;37: 1863-1878.

[19] Harper L.T., Turner, T.A., Warrior N.A., Dahi J.S., Rudd C.D. Characterisation of random carbon fibre composites from adirected fibre preforming process: analysis of microstructural parameters. Compos Part A-Appl S. 2006;37: 2136-2147.

[20] Qian C., Harper L.T., Turner T.A., Warrior N.A. Notched behaviour of discontinuous carbon fibre composites: Comparisonwith quasi-isotropic non-crimp fabric. Compos Part A-Appl S. 2011;42: 293-302.

[21] Goidescu C., Welemane H., Garnier C., Fazzini M., Brault R.,Peronnet E., Mistou S. Damage investigation in CFRP composites using full-field measurementtechniques: combination of digital image stereo-correlation, infraredthermography and X-ray tomography. Compos Part B-Eng. 2013;48: 95-105.

[22] Selezneva M., Roy S., Lessard L., Yousefpour A. Analytical model for prediction of strength and fracture pathscharacteristic to randomly oriented strand (ROS) composites. Compos Part B-Eng. 2016;96: 103-111.

[23] Selezneva M., Roy S., Meldrum S., Lessard L., Yousefpour A. Modelling of mechanical propertiesof randomly oriented strandthermoplastic composites. J Compos Mater. 2016;0: 1-15.

[24] Li Y., Chen Z., Xu H., Dahl J., Zeng D., Mirdamadi M., Su X. Modeling and Simulation of Compression Molding Process for Sheet Molding Compound (SMC) of Chopped Carbon Fiber Composites. SAE Int J Mater Manf. 2017;10: 130-137.

[25] ASTM D3039/D3039M-14. Tensile properties of polymer matrix composite materials.

[26] Lomov S.V. Ivanov D.S., Truong T.C., Verpoest I., Baudry F., Vanden Boshe K., Xie H. Experimental methodology of study of damage initiation and development in textile composites in uniaxial tensile test. Compos Sci Technol. 2008;68: 2340-2349.

[27] Hong L., Wan Y., Jain A.K. Fingerprint image enhancement:Algorithm and performance evaluation. IEEE Transactions on Pattern Analysis and Machine Intelligence. 1998;20: 777-789.

[28] Peter K. Phase Preserving Tone Mapping of Non-Photographic High Dynamic Range Images. Proceedings: The Australian Pattern Recognition Society Conference: Digital Image Computing: Techniques and Applications DICTA. 2012.

[29] Advani S.G., Tucker C.L. The use of tensors to describe and predict fiber orientation in short fiber composites. J Rheol. 1987;31: 751-784.

Author Manuscript

This article is protected by copyright. All rights reserved.

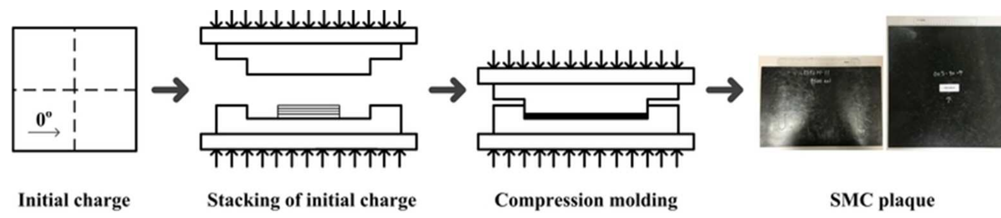

Figure 1. Manufacturing processing of SMC plaqu

65x13mm (300 x 300 DPI)

Author Manus

This article is protected by copyright. All rights reserved.

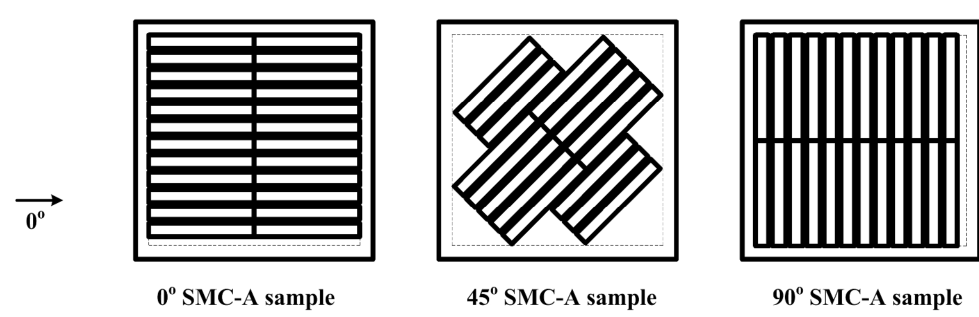

Figure 2. The schematic of samples cut from SMC-A plaques

270x85mm (300 x 300 DPI)

Author Manu

This article is protected by copyright. All rights reserved.

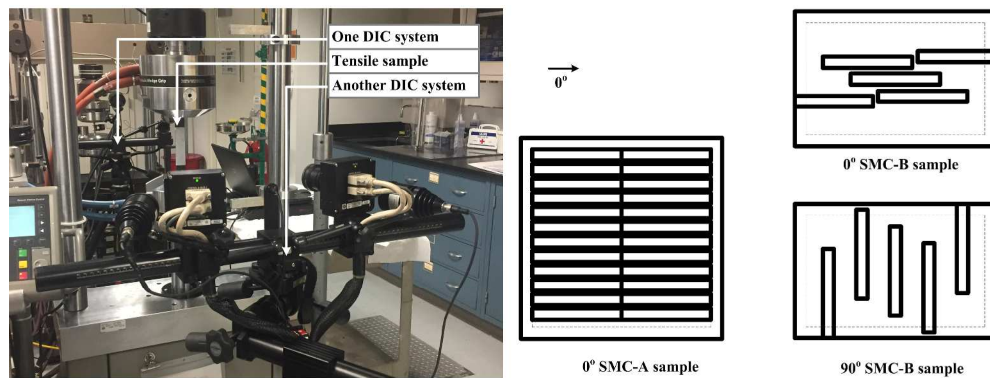

Figure 3. Tensile test set-up with two DIC systems

415x156mm (300 x 300 DPI)

Author Man

This article is protected by copyright. All rights reserved.

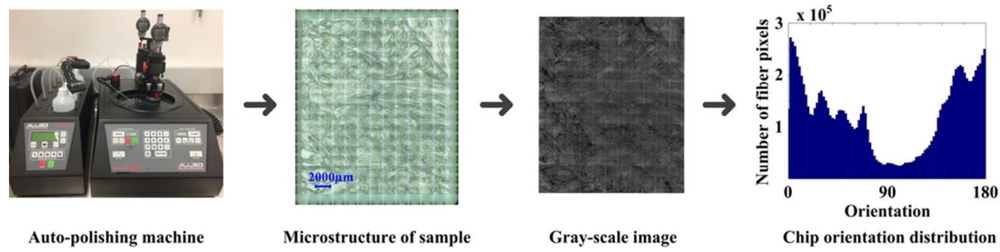

Figure 4. Automatic polishing and image processing

90x22mm (300 x 300 DPI)

Author Manuscript

This article is protected by copyright. All rights reserved.

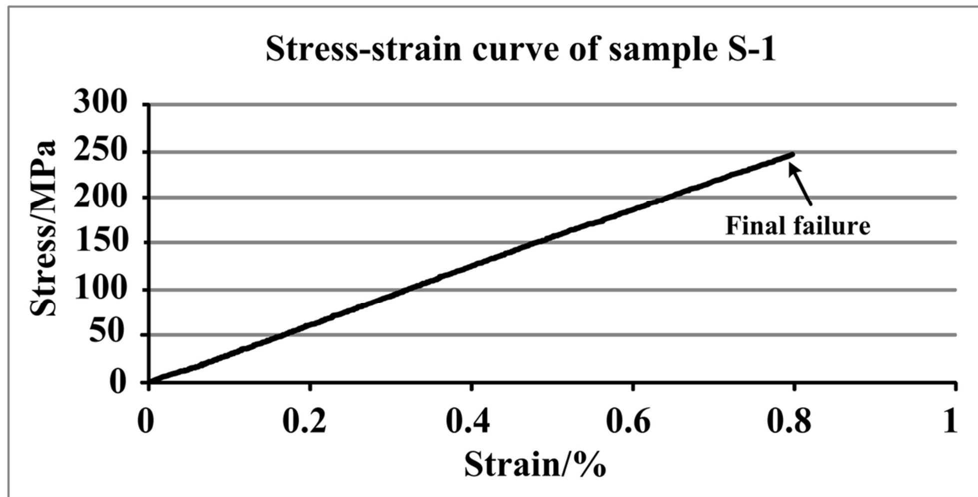

Figure 5. Representative stress-strain curve for the whole bar of SMC-A samples

118x60mm (300 x 300 DPI)

Author Ma

This article is protected by copyright. All rights reserved.

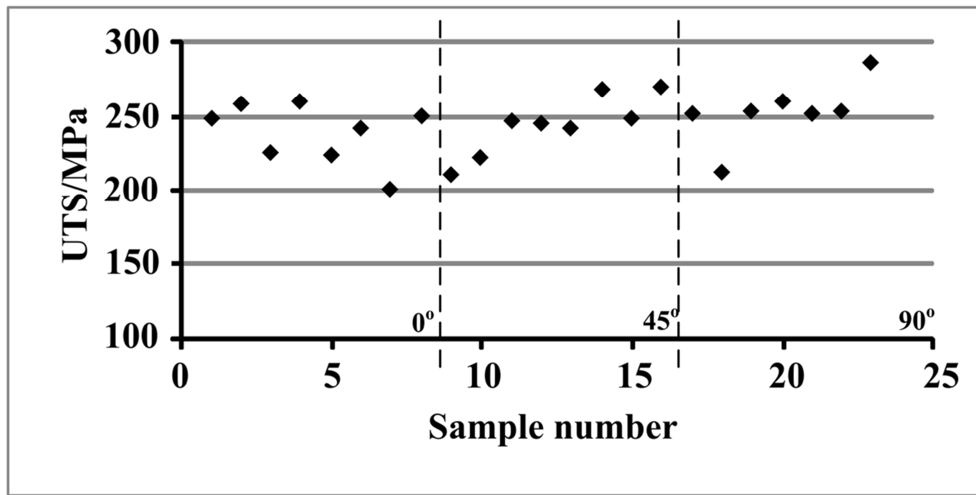

Figure 6. UTS for SMC-A samples

118x60mm (300 x 300 DPI)

Author Ma

This article is protected by copyright. All rights reserved.

Full strain field of typical tensile sample S-1

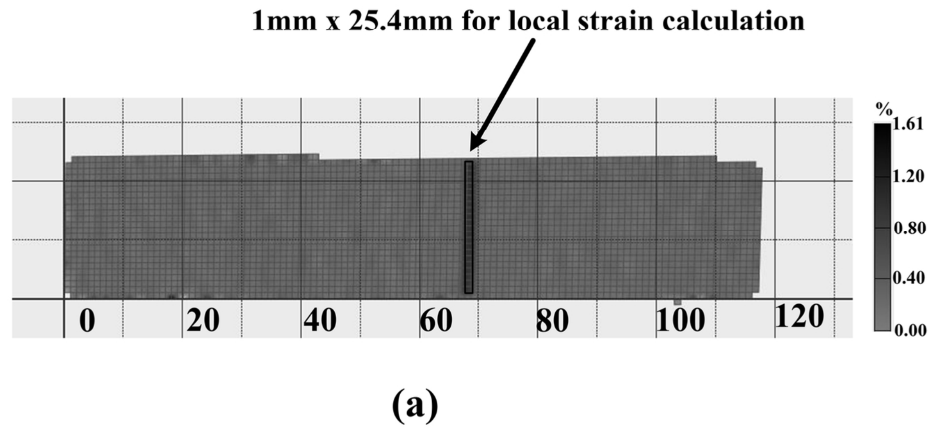

Figure 7. Representative SMC-A samples analysis with strain localization and failure location for (a) an overview of local strain calculation

125x76mm (300 x 300 DPI)

Author M

This article is protected by copyright. All rights reserved.

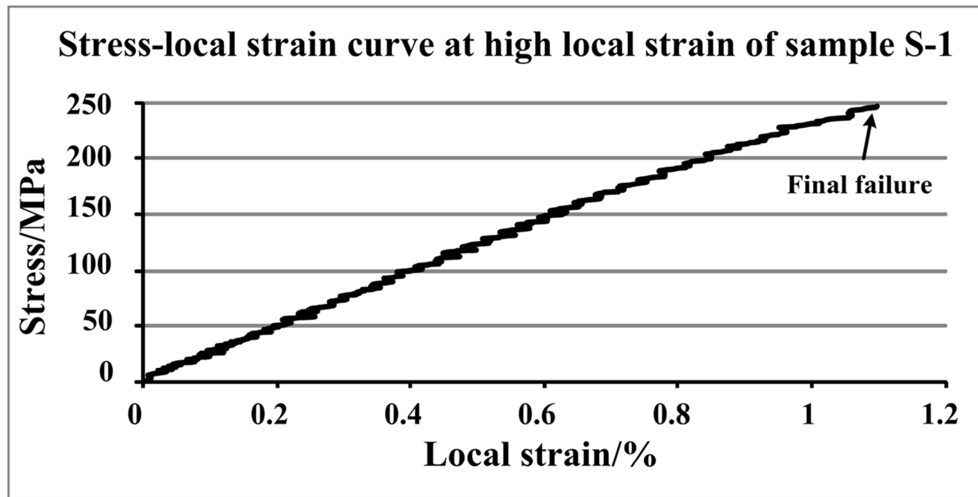

Figure 7. Representative SMC-A samples analysis with strain localization and failure location for (b) stress-local strain curve at high strain area

128x71mm (300 x 300 DPI)

Author Ma

This article is protected by copyright. All rights reserved.

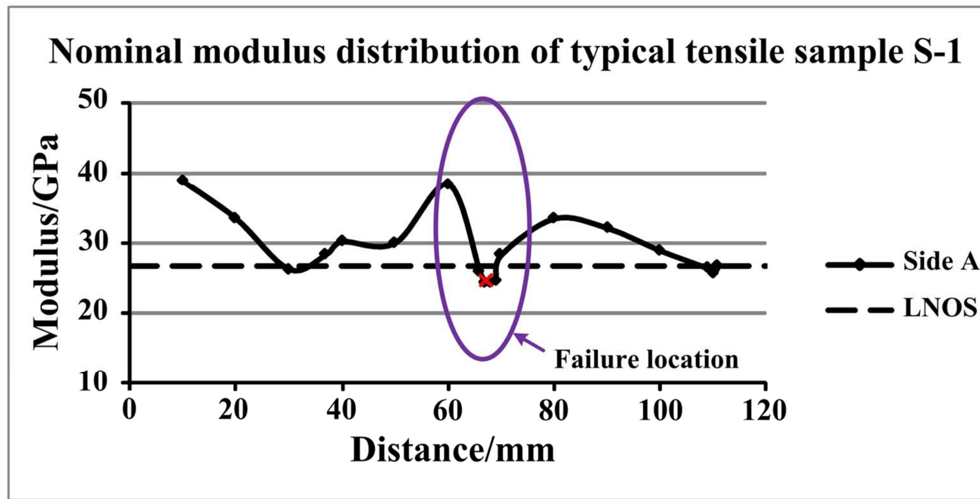

(c)

Figure 7. Representative SMC-A samples analysis with strain localization and failure location for (c) sample S-1

129x73mm (300 x 300 DPI)

Author M

This article is protected by copyright. All rights reserved.

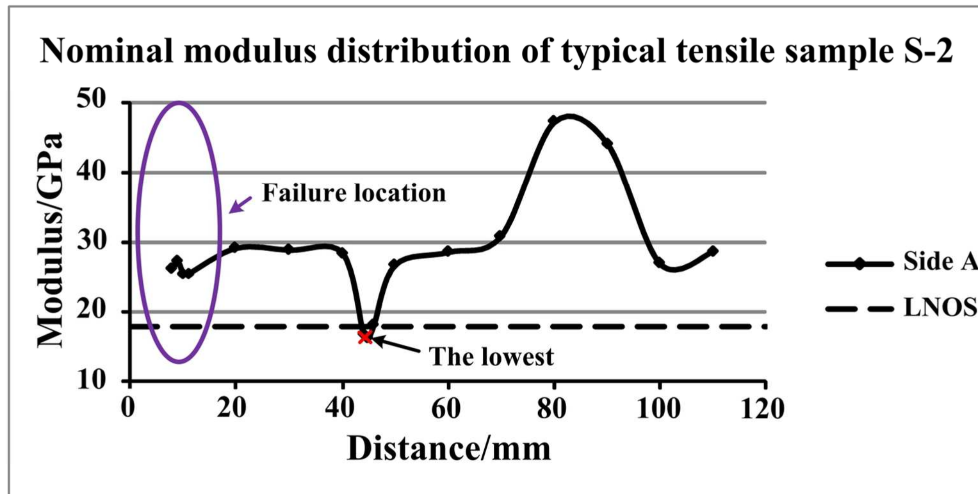

(d)

Figure 7. Representative SMC-A samples analysis with strain localization and failure location for (d) sample S-2.

129x72mm (300 x 300 DPI)

Author M

This article is protected by copyright. All rights reserved.

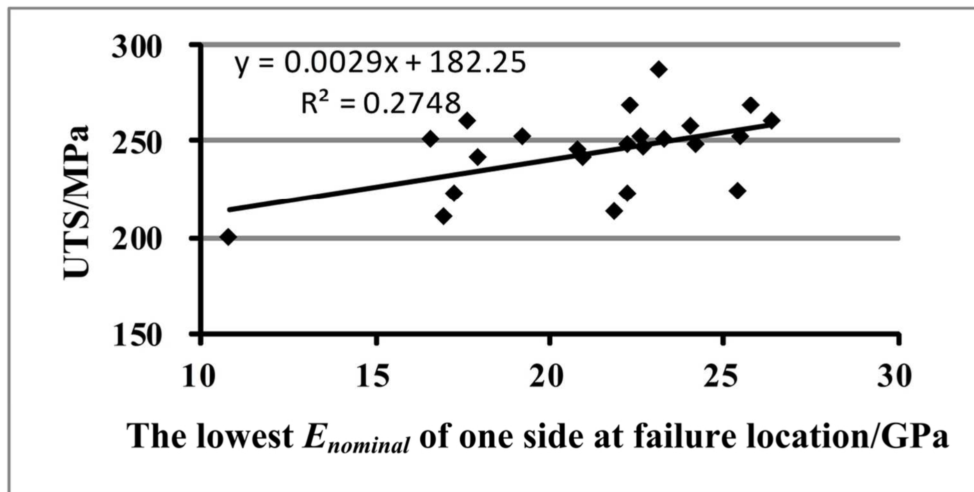

Figure 8. Relationship between UTS and the lowest Enominal of one side at failure location for SMC-A materials

118x60mm (300 x 300 DPI)

Author Ma

This article is protected by copyright. All rights reserved.

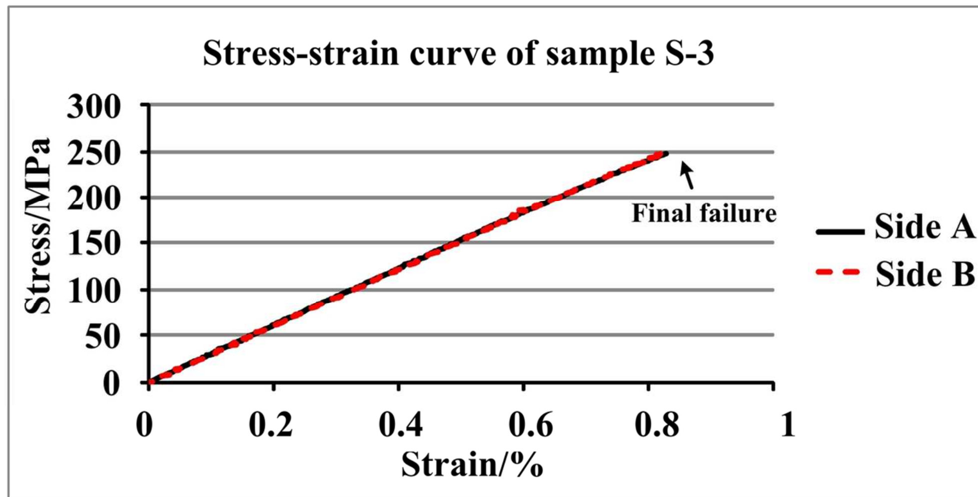

Figure 9. Representative stress-strain curves for the whole bar of SMC-A samples from two opposing sides

118x60mm (300 x 300 DPI)

Author Ma

This article is protected by copyright. All rights reserved.

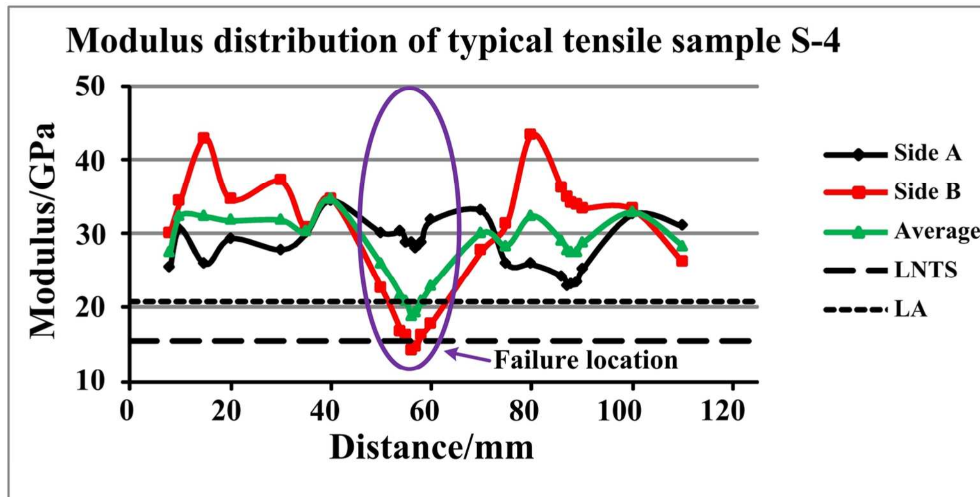

(a)

Figure 10. Representative SMC-A samples analysis with strain localization and failure location for (a) sample S-4

129x72mm (300 x 300 DPI)

Author Ma

This article is protected by copyright. All rights reserved.

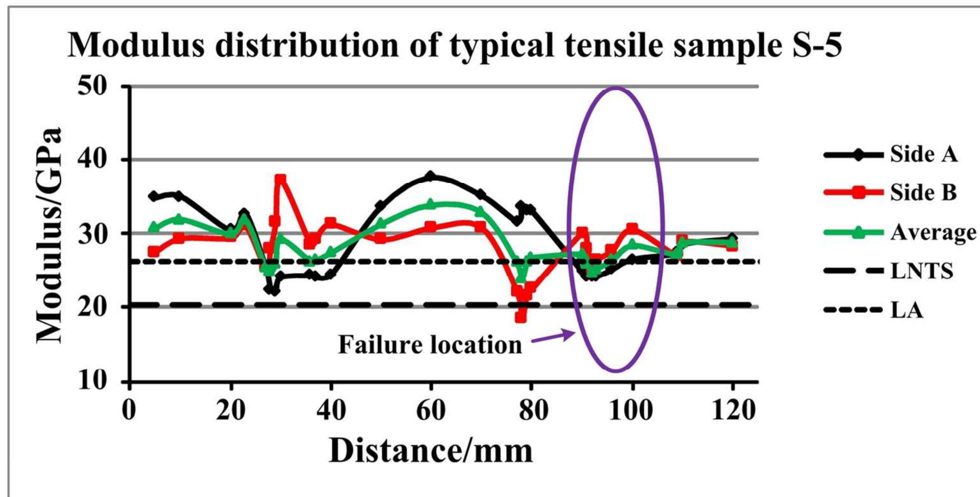

(b)

Figure 10. Representative SMC-A samples analysis with strain localization and failure location for (b) sample S-5

129x72mm (300 x 300 DPI)

Author Ma

This article is protected by copyright. All rights reserved.

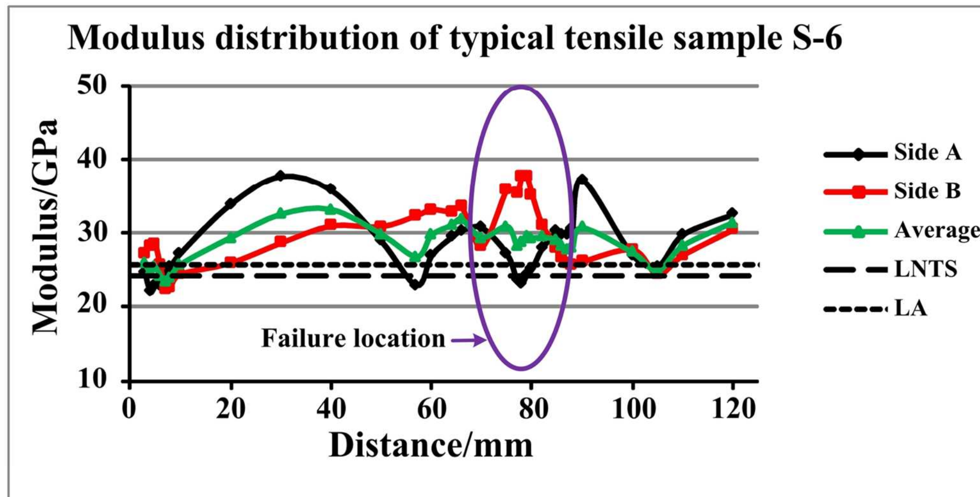

(c)

Figure 10. Representative SMC-A samples analysis with strain localization and failure location for (c) sample S-6

130x73mm (300 x 300 DPI)

Author Manuscript

This article is protected by copyright. All rights reserved.

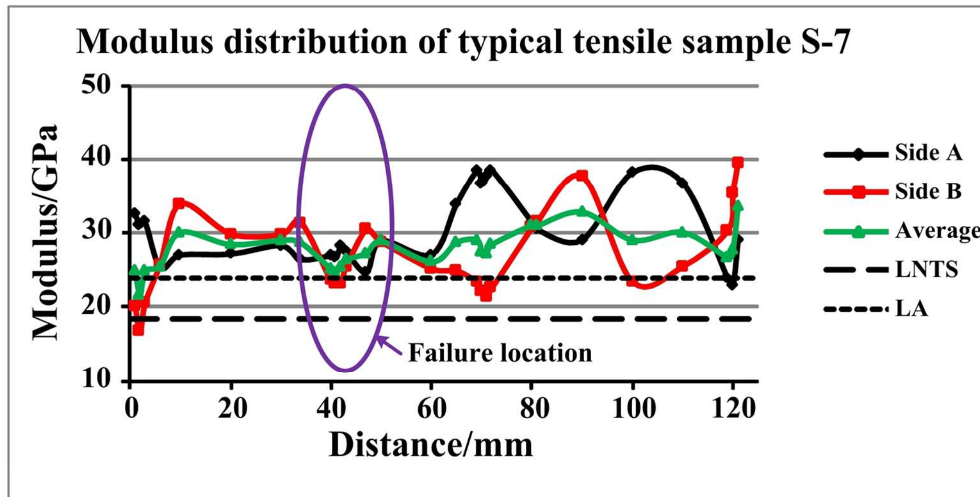

(d)

Figure 10. Representative SMC-A samples analysis with strain localization and failure location for (d) sample S-7

130x73mm (300 x 300 DPI)

Author M

This article is protected by copyright. All rights reserved.

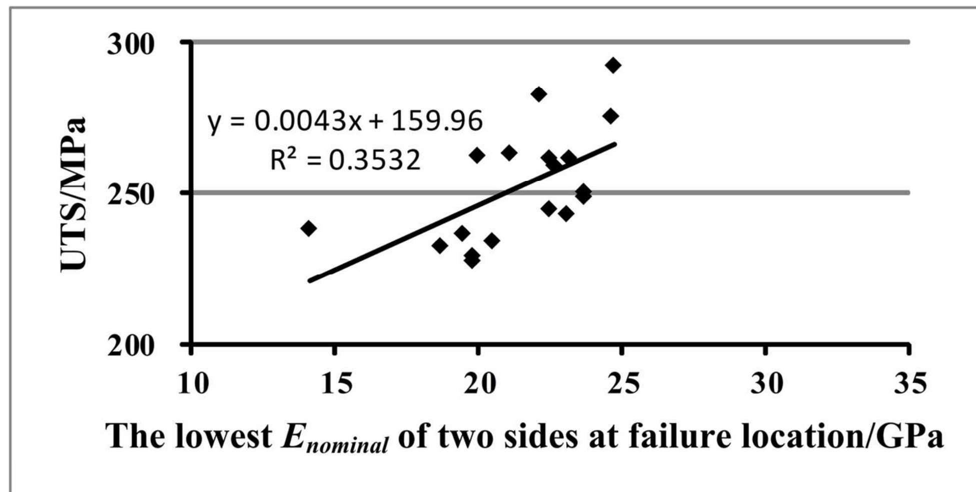

(a)

Figure 11. Relationship between UTS and modulus for SMC-A materials for (a) the lowest Enominal of two sides at failure location

129x72mm (300 x 300 DPI)

Author M

This article is protected by copyright. All rights reserved.

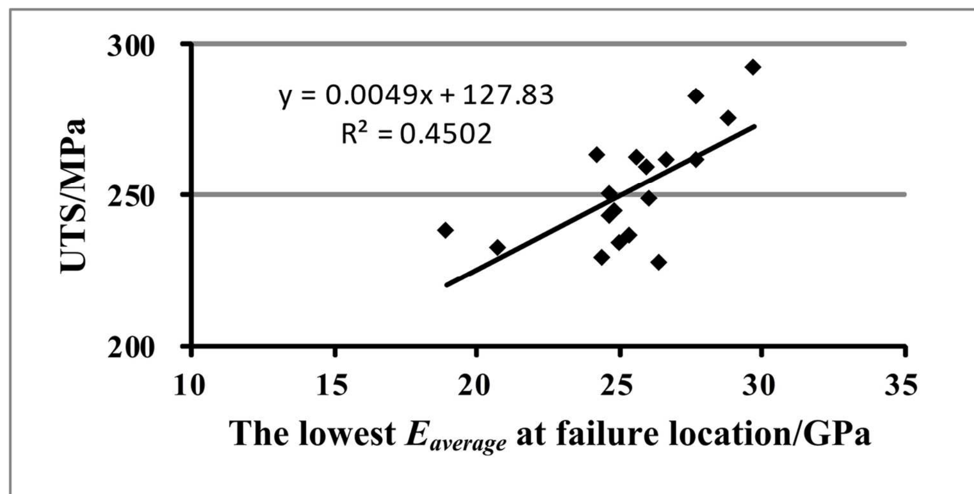

(b)

Figure 11. Relationship between UTS and modulus for SMC-A materials for (b) the lowest Eaverage at failure location

129x72mm (300 x 300 DPI)

Author Ma

This article is protected by copyright. All rights reserved.

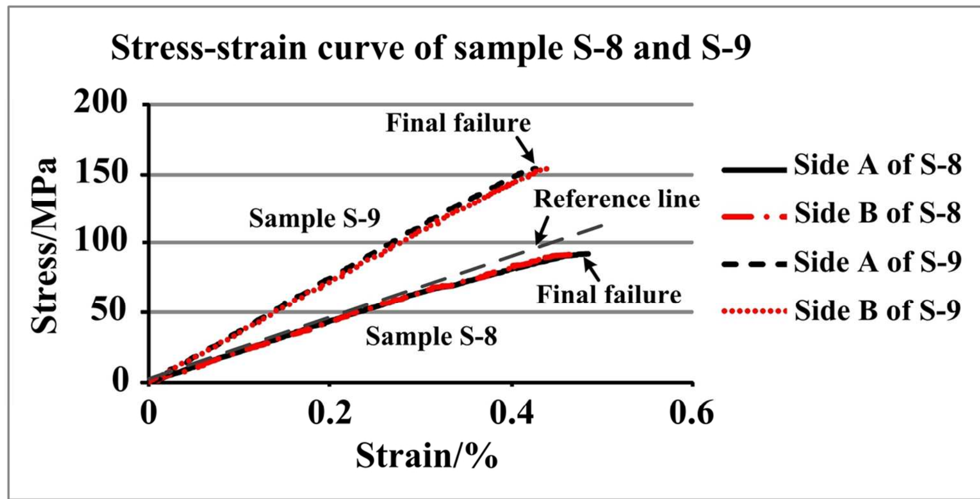

Figure 12. Representative stress-strain curves for the whole bar of SMC-B samples from two opposing sides

118x60mm (300 x 300 DPI)

Author Ma

This article is protected by copyright. All rights reserved.

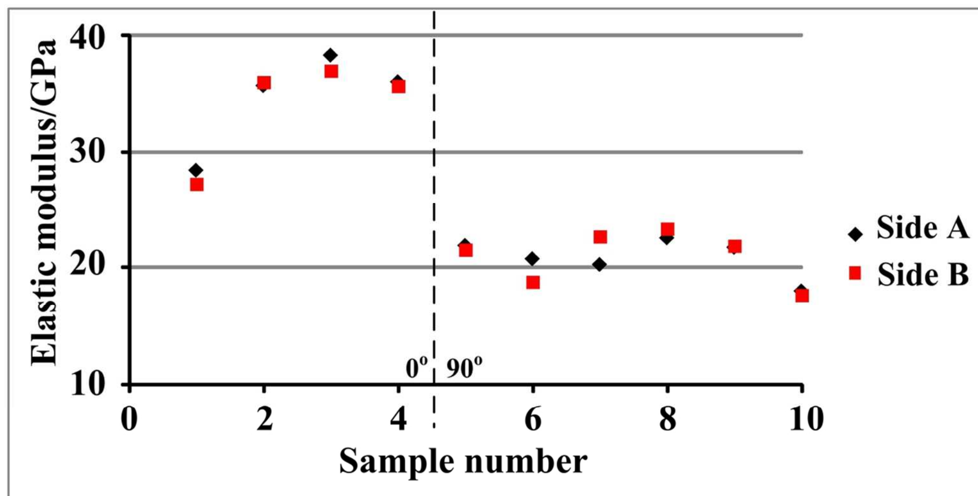

Figure 13. Global modulus for SMC-B materials

118x60mm (300 x 300 DPI)

Author Ma

This article is protected by copyright. All rights reserved.

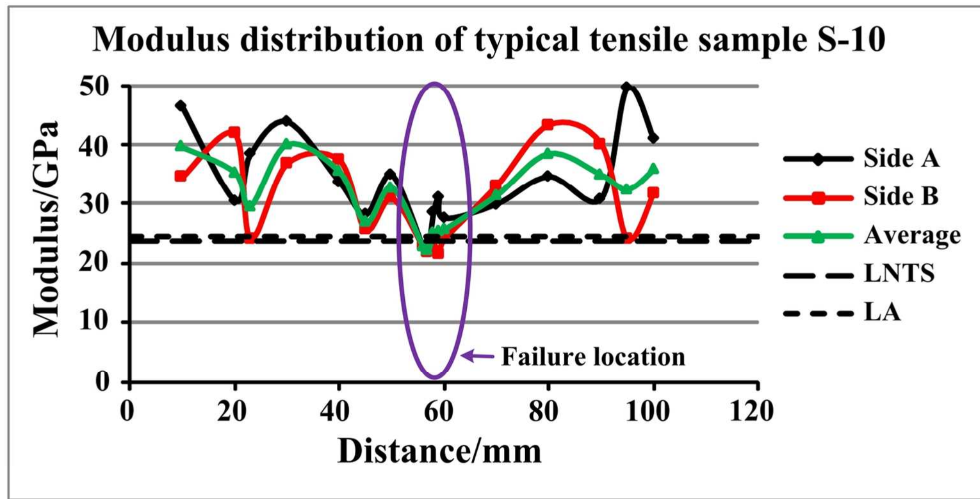

(a)

Figure 14. Representative SMC-B samples analysis with strain localization and failure location for (a) sample S-10

129x73mm (300 x 300 DPI)

Author Ma

This article is protected by copyright. All rights reserved.

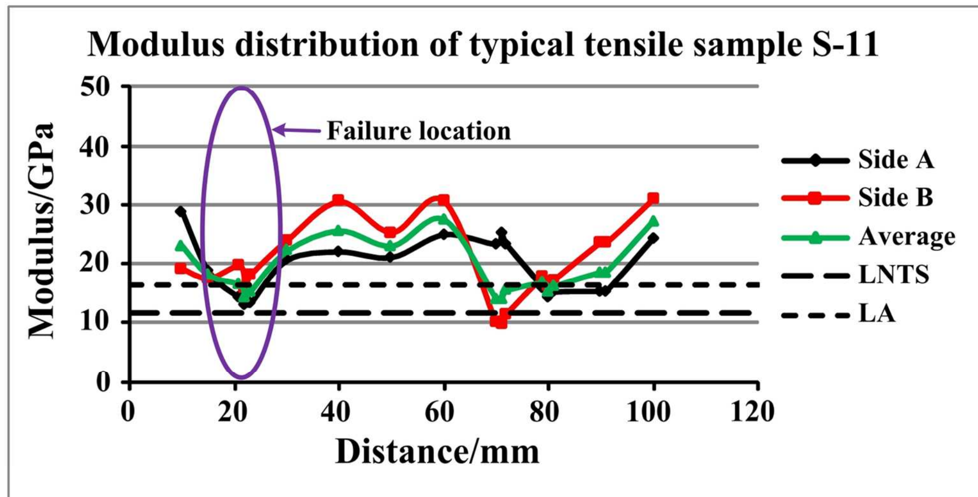

(b)

Figure 14. Representative SMC-B samples analysis with strain localization and failure location for (b) sample S-11

129x73mm (300 x 300 DPI)

Author Manuscript

This article is protected by copyright. All rights reserved.

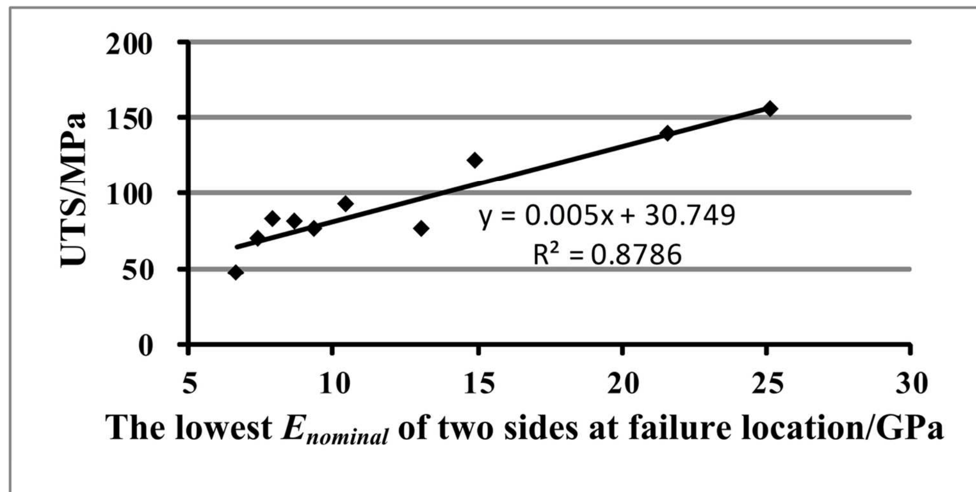

(a)

Figure 15. Relationship between UTS and modulus for SMC-B materials for (a) the lowest Enominal of two sides at failure location

129x72mm (300 x 300 DPI)

Author Ma

This article is protected by copyright. All rights reserved.

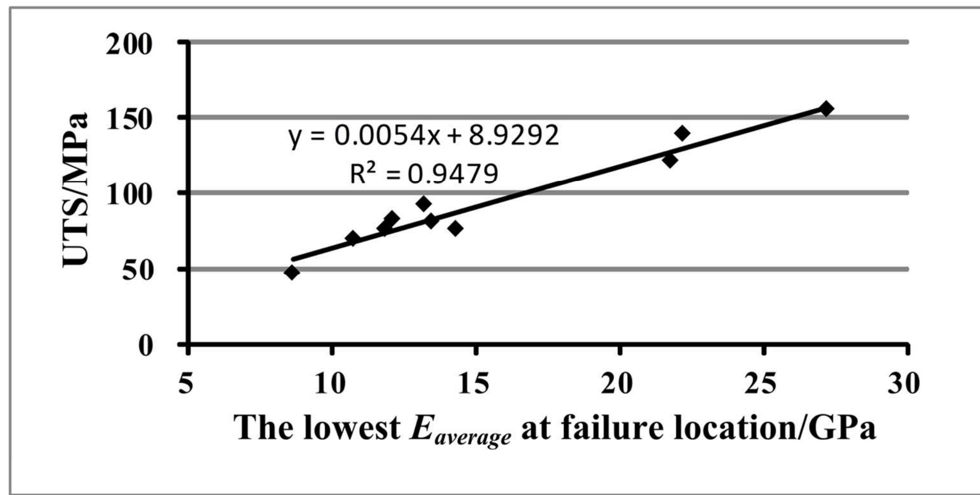

(b)

Figure 15. Relationship between UTS and modulus for SMC-B materials for (b) the lowest Eaverage at failure location

129x72mm (300 x 300 DPI)

Author M

This article is protected by copyright. All rights reserved.

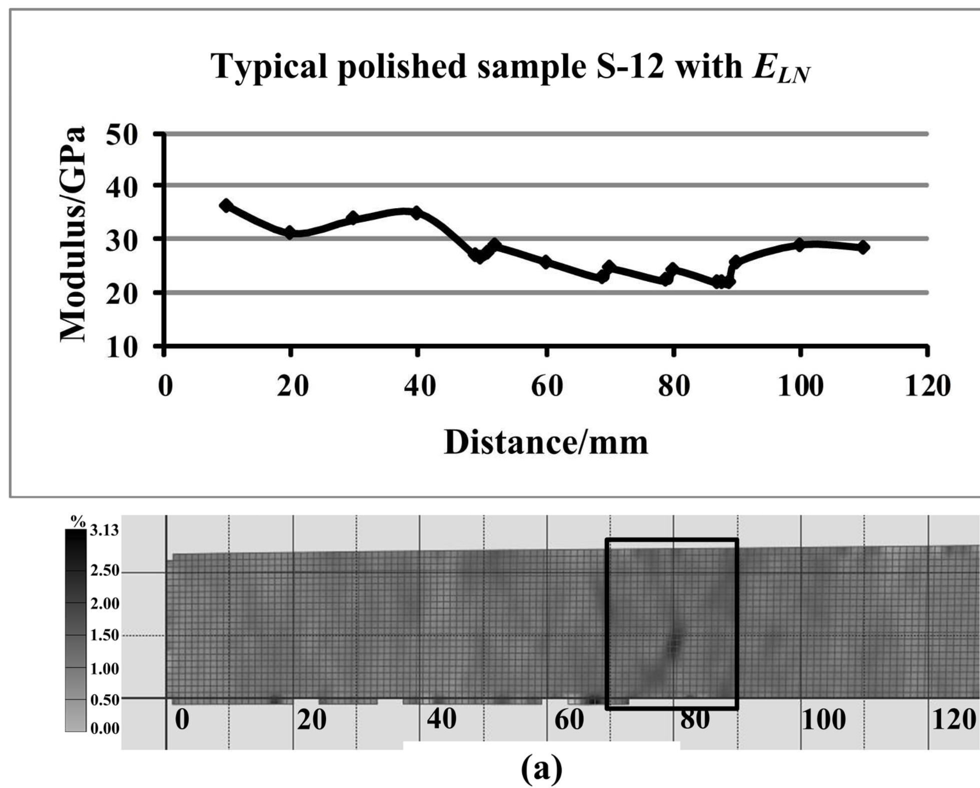

Figure 16. Representative sample for microstructure analysis for (a) sample S-12 with ELN

184x146mm (300 x 300 DPI)

Author

This article is protected by copyright. All rights reserved.

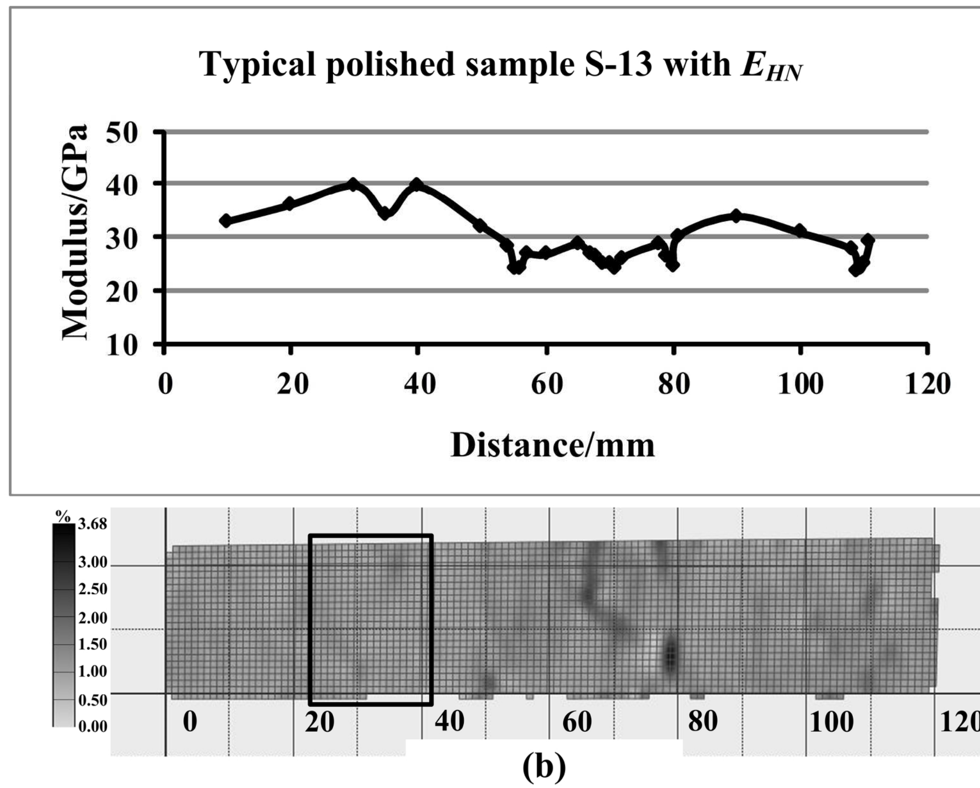

Figure 16. Representative sample for microstructure analysis for(b) sample S-13 with EHN

184x146mm (300 x 300 DPI)

Author

This article is protected by copyright. All rights reserved.

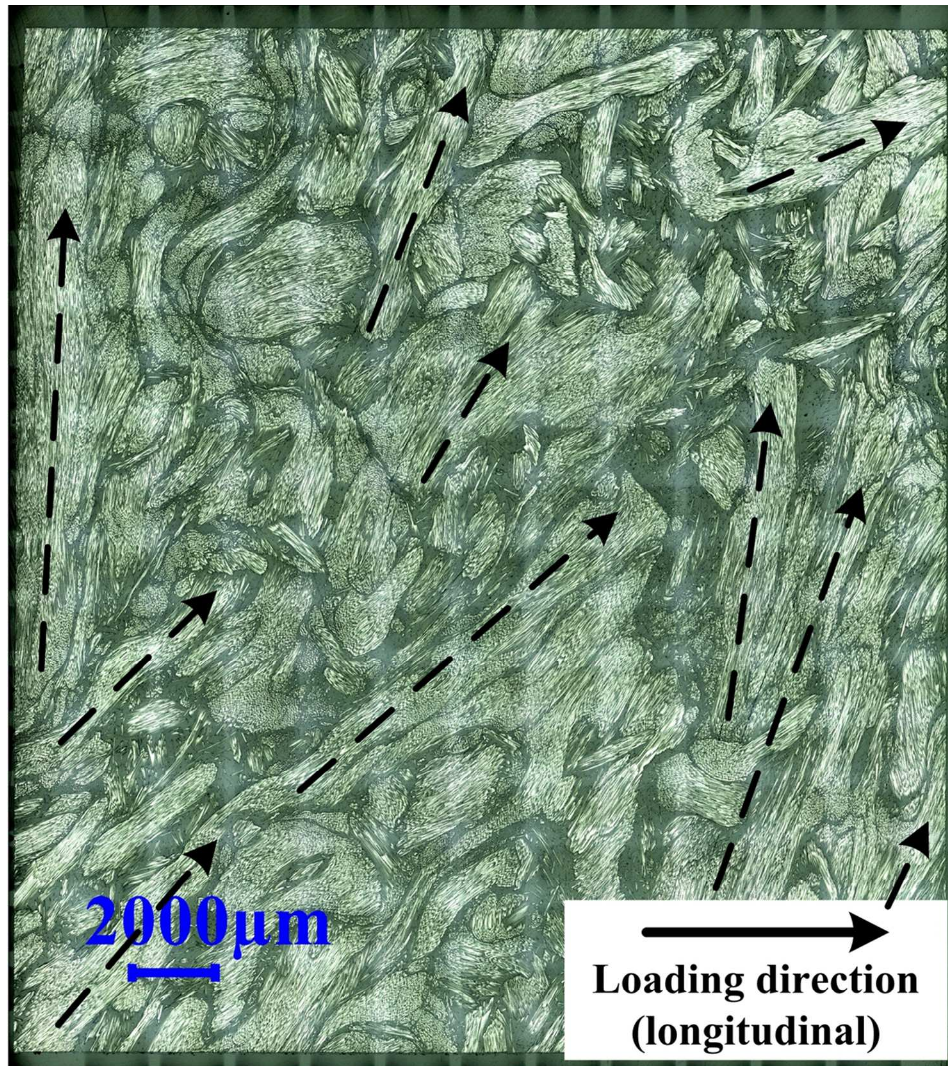

One typical layer in sample S-12

(a)

Figure 17. Typical microstructures for sample in Figure 16 for (a) sample S-12 with ELN

98x124mm (300 x 300 DPI)

Au

This article is protected by copyright. All rights reserved.

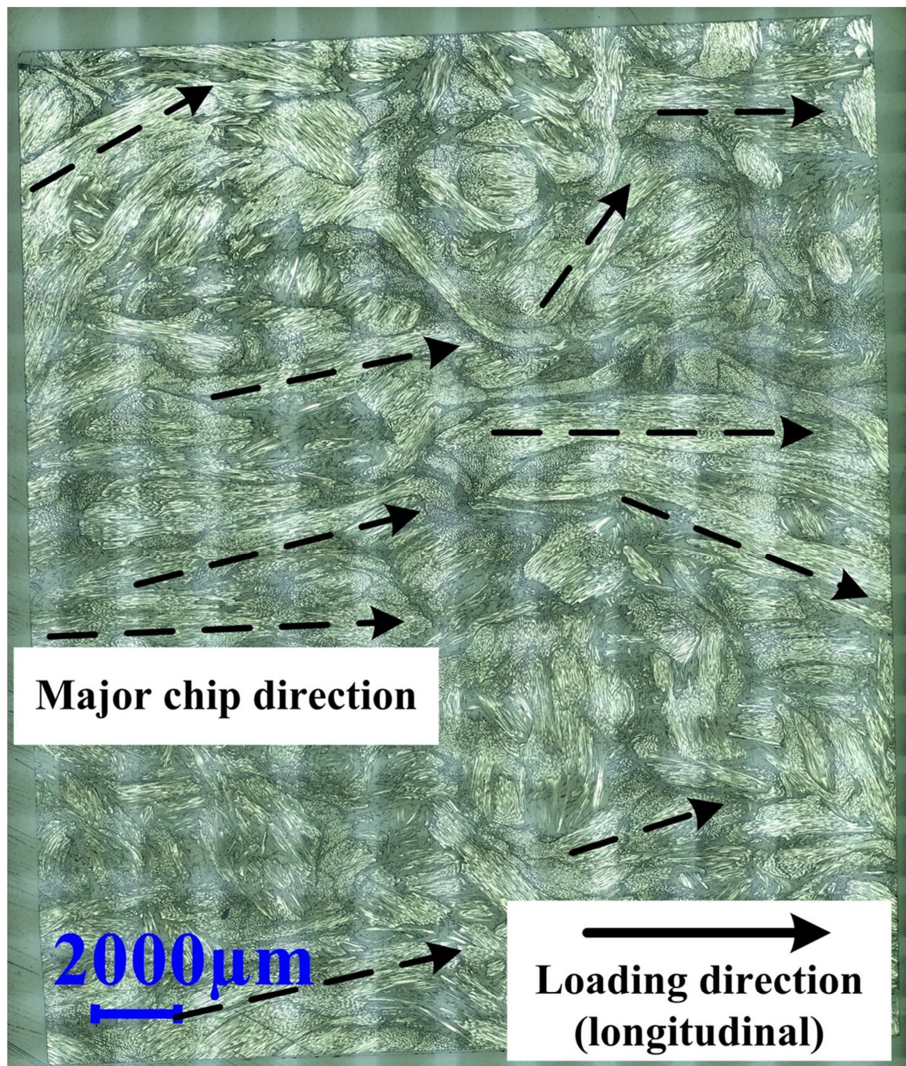

One typical layer in sample S-13

(b)

Figure 17. Typical microstructures for sample in Figure 16 for (b) sample S-13 with EHN

98x131mm (300 x 300 DPI)

Au

This article is protected by copyright. All rights reserved.

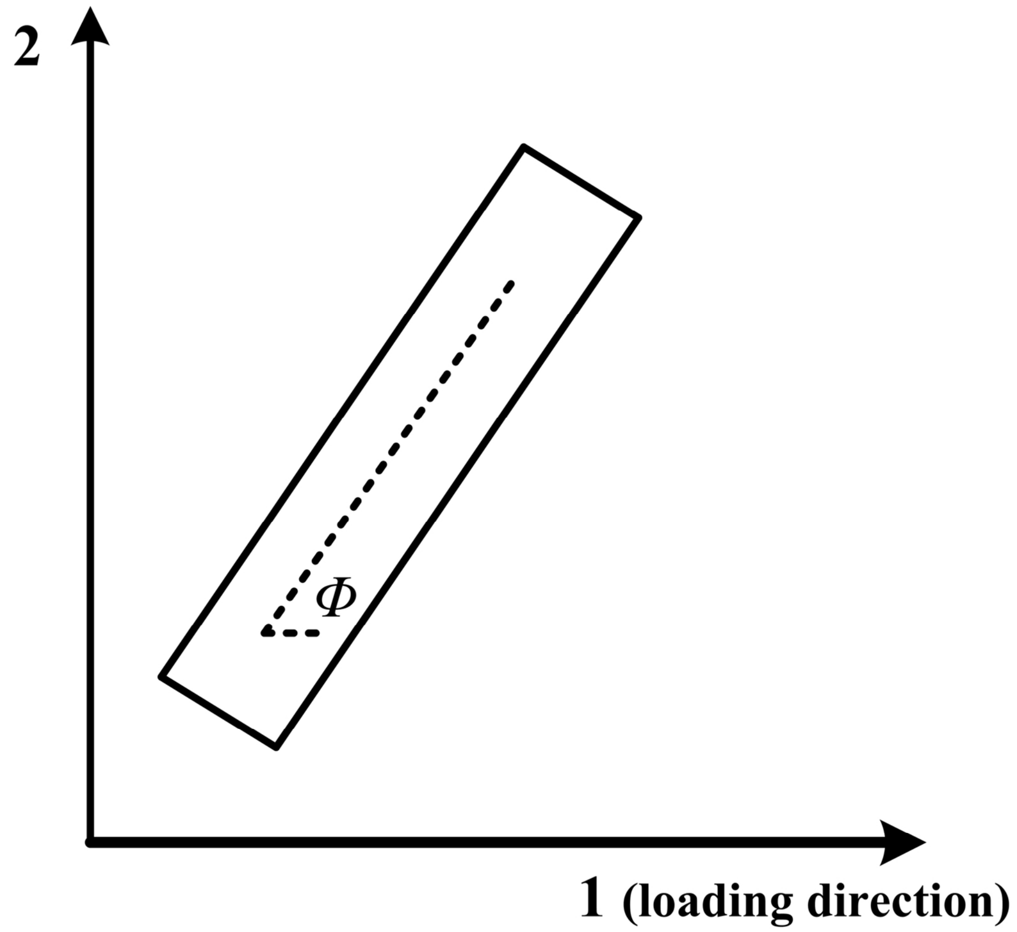

Figure 18. Coordinate system and definition of Φ

66x61mm (600 x 600 DPI)

Autho

This article is protected by copyright. All rights reserved.

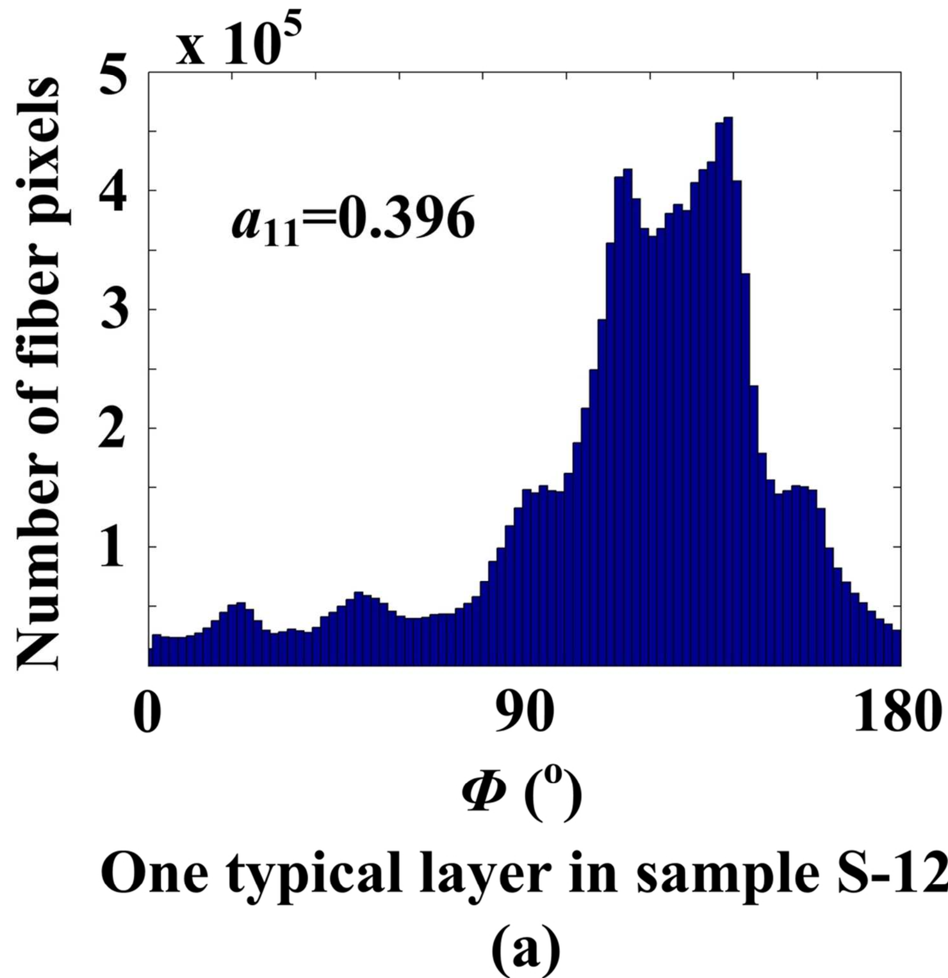

Figure 19. Chip orientation distribution and the calculated a11 components of the fiber orientation tensors of images in Figure 17 for (a) sample S-12 with ELN

103x104mm (300 x 300 DPI)

This article is protected by copyright. All rights reserved.

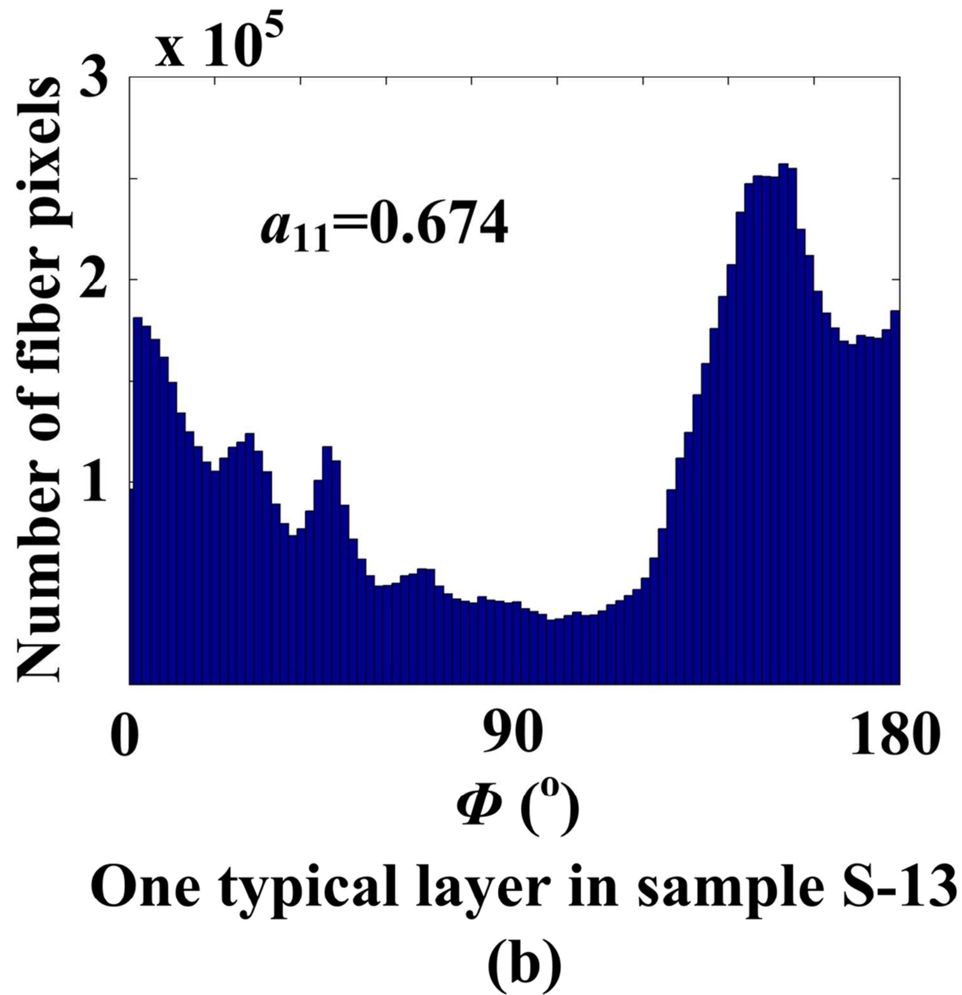

Figure 19. Chip orientation distribution and the calculated a11 components of the fiber orientation tensors of images in Figure 17 for (b) sample S-13 with EHN

103x106mm (300 x 300 DPI)

Auth

This article is protected by copyright. All rights reserved.

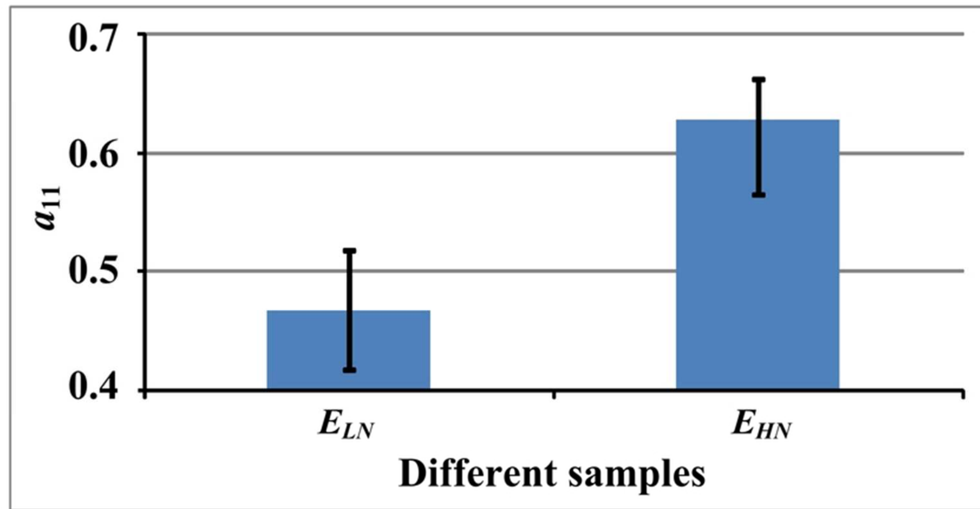

Figure 20. Relationship between average a11 and Enominal

71x37mm (300 x 300 DPI)

Author Ma

This article is protected by copyright. All rights reserved.

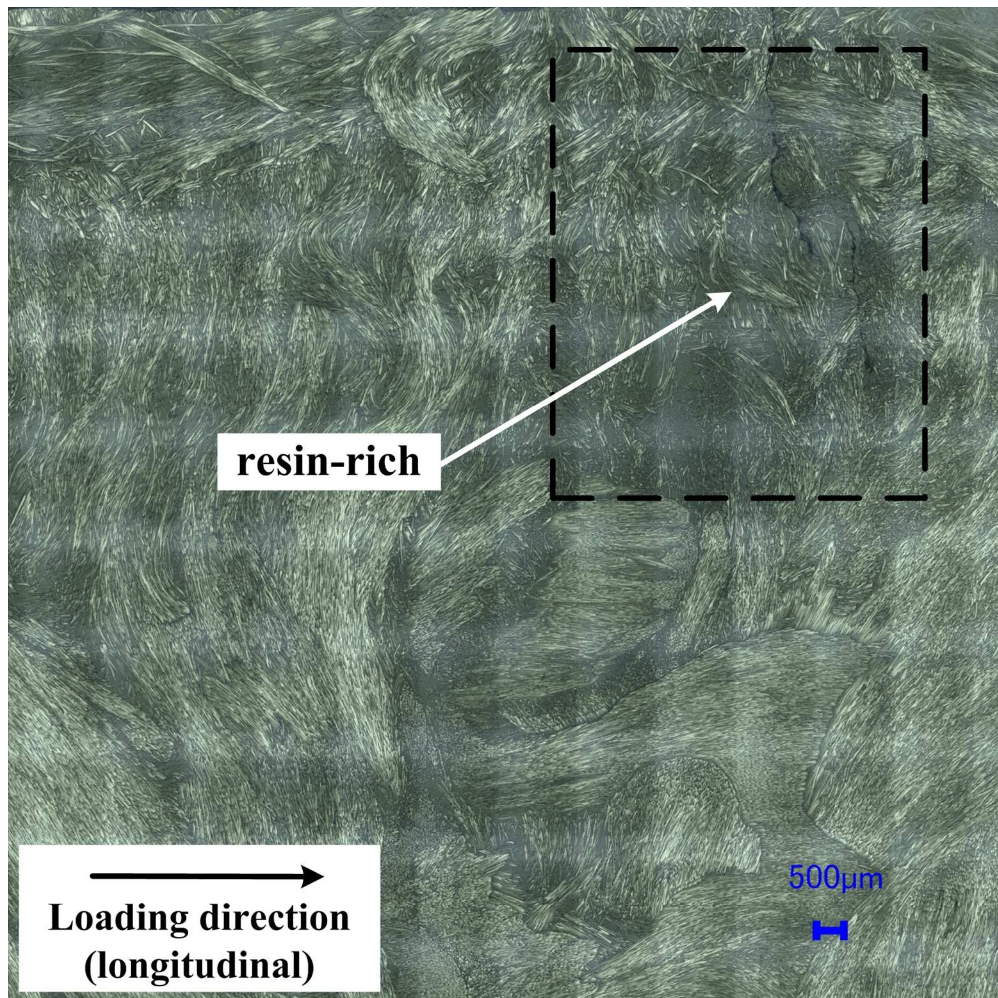

Figure 21. Resin-rich region in SMC-B materials

142x142mm (300 x 300 DPI)

Auth

This article is protected by copyright. All rights reserved.

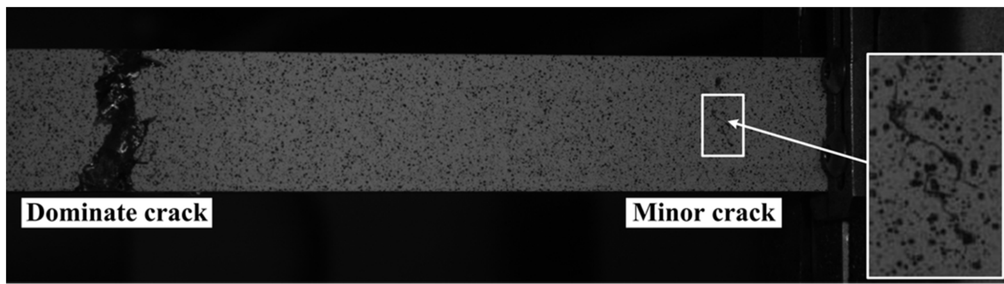

Figure 22. Dominate and minor cracks

88x24mm (300 x 300 DPI)

Author Manu

This article is protected by copyright. All rights reserved.

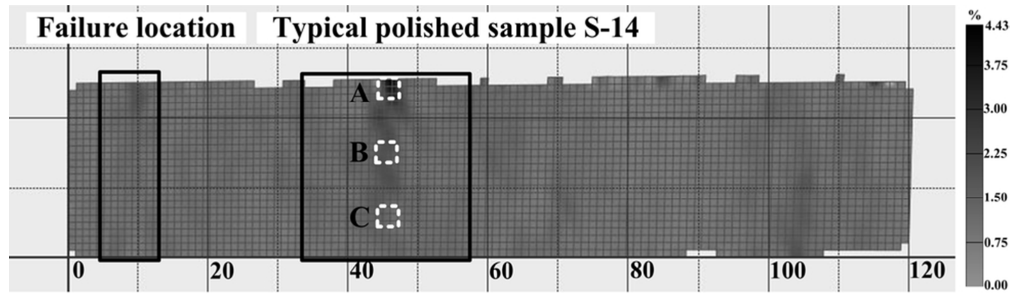

Figure 23. Typical sample for failure analysis

82x23mm (300 x 300 DPI)

Author Manu

This article is protected by copyright. All rights reserved.

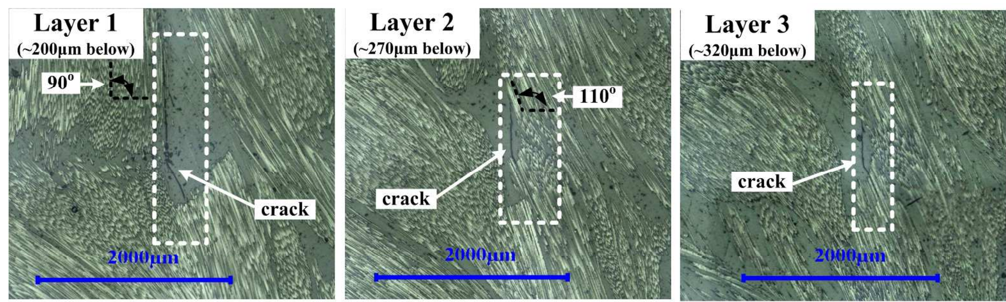

Figure 24. Crack initiation and initial propagation at different locations in sample S-14 for (a) location A

244x82mm (300 x 300 DPI)

Author Manu

This article is protected by copyright. All rights reserved.

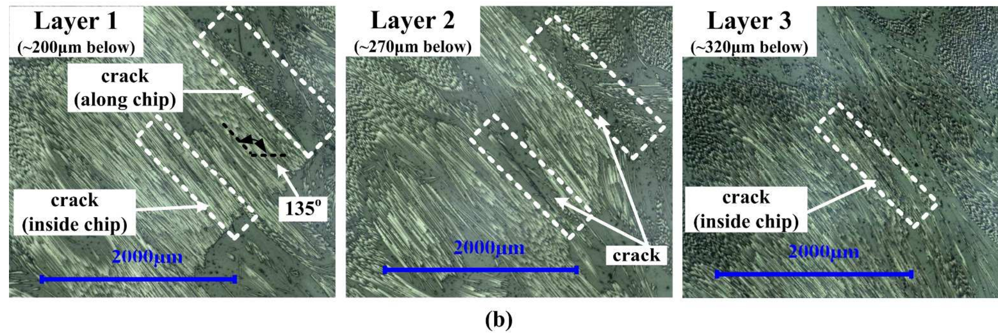

(b)

Figure 24. Crack initiation and initial propagation at different locations in sample S-14 for (b) location B

245x82mm (300 x 300 DPI)

Author Manuscript

This article is protected by copyright. All rights reserved.

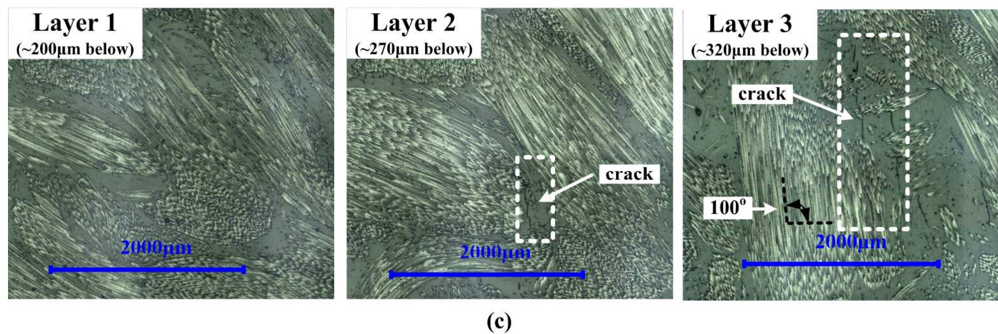

Figure 24. Crack initiation and initial propagation at different locations in sample S-14 for (c) location C

245x83mm (300 x 300 DPI)

Author Manuscript

This article is protected by copyright. All rights reserved.

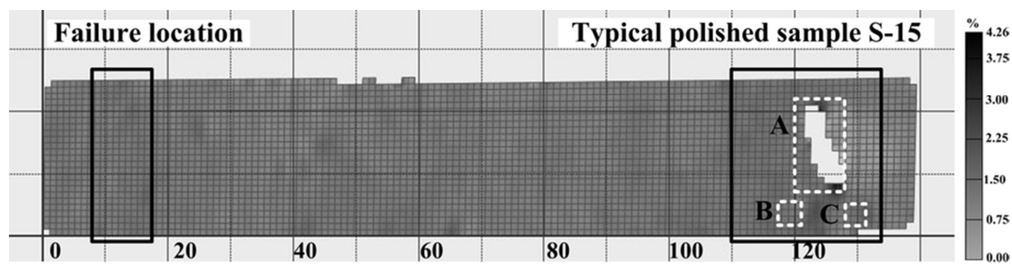

Figure 25. Typical polished sample S-15

77x19mm (300 x 300 DPI)

Author Manus

This article is protected by copyright. All rights reserved.

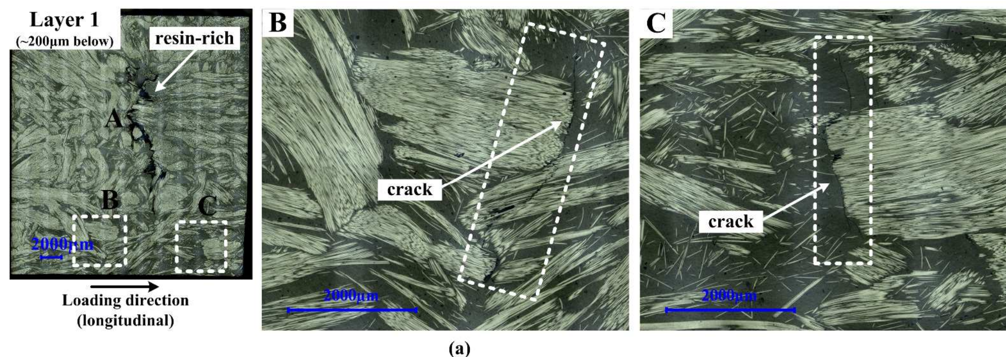

Figure 26. Microstructure of sample S-15 at different layers for (a) layer 1

294x107mm (300 x 300 DPI)

Author Manuscript

This article is protected by copyright. All rights reserved.

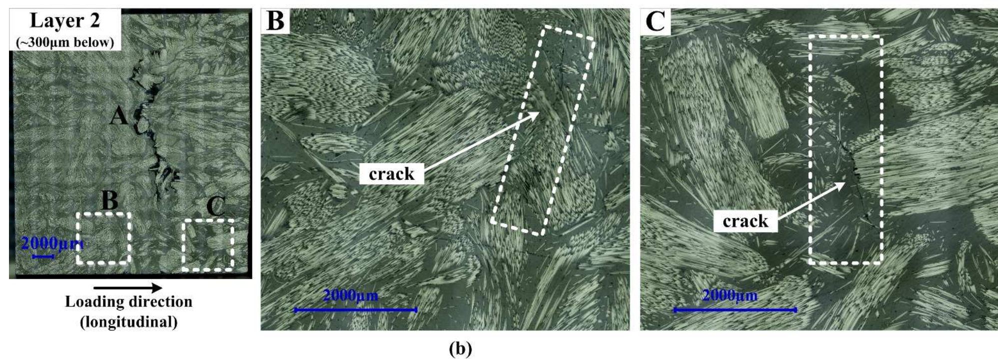

Figure 26. Microstructure of sample S-15 at different layers for (b) layer 2

293x107mm (300 x 300 DPI)

Author Man

This article is protected by copyright. All rights reserved.

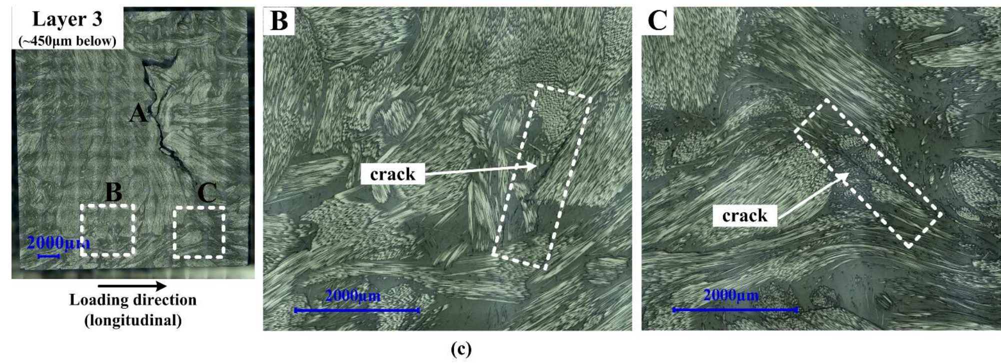

Figure 26. Microstructure of sample S-15 at different layers for (c) layer 3

294x107mm (300 x 300 DPI)

Author Man

This article is protected by copyright. All rights reserved.

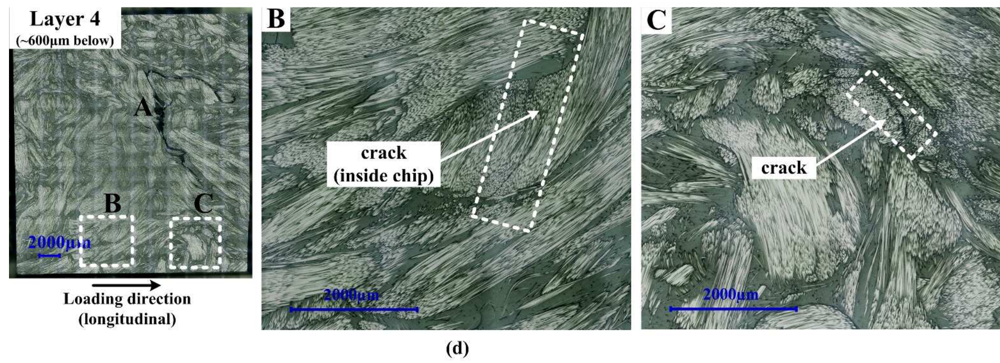

Figure 26. Microstructure of sample S-15 at different layers for (d) layer 4

294x108mm (300 x 300 DPI)

Author Manuscript

This article is protected by copyright. All rights reserved.